The Astrophysical Journal, 833:246 (15pp), 2016 December 20 doi:10.3847/1538-4357/833/2/246

THE PHYSICAL ENVIRONMENT AROUND IRAS 17599–2148: INFRARED DARK CLOUD AND BIPOLAR NEBULA

L. K. Dewangan[1], D. K. Ojha[2], I. Zinchenko[3], P. Janardhan[1], S. K. Ghosh[4], and A. Luna[5]
[1] Physical Research Laboratory, Navrangpura, Ahmedabad 380 009, India; lokeshd@prl.res.in
[2] Department of Astronomy and Astrophysics, Tata Institute of Fundamental Research, Homi Bhabha Road, Mumbai 400 005, India
[3] Institute of Applied Physics of the Russian Academy of Sciences, 46 Ulyanov st., Nizhny Novgorod 603950, Russia
[4] National Centre for Radio Astrophysics, Ganeshkhind, Pune 411 007, India
[5] Instituto Nacional de Astrofísica, Óptica y Electrónica, Luis Enrique Erro # 1, Tonantzintla, Puebla, C.P. 72840, México
Received 2016 August 4; revised 2016 October 14; accepted 2016 October 26; published 2016 December 20

ABSTRACT

We present a multiscale and multiwavelength study to investigate the star formation process around IRAS 17599–2148, which is part of an elongated filamentary structure (EFS) (extension ∼21 pc) seen in the *Herschel* maps. Using the *Herschel* data analysis, at least six massive clumps ($M_{\rm clump}$ ∼ 777–7024 $M_{\odot}$) are found in the EFS with a range of temperature and column density of ∼16–39 K and ∼(0.6–11) × 10^{22} cm^{-2} (A_V ∼ 7–117 mag), respectively. The EFS hosts cold gas regions (i.e., infrared dark cloud) without any radio detection and a bipolar nebula (BN) linked with the H II region IRAS 17599–2148, tracing two distinct environments inferred through the temperature distribution and ionized emission. Based on virial analysis and higher values of self-gravitating pressure, the clumps are found unstable against gravitational collapse. We find 474 young stellar objects (YSOs) in the selected region, and ∼72% of these YSOs are found in the clusters distributed mainly toward the clumps in the EFS. These YSOs might have spontaneously formed due to processes not related to the expanding H II region. At the edges of BN, four additional clumps are also associated with YSO clusters, which appear to be influenced by the expanding H II region. The most massive clump in the EFS contains two compact radio sources traced in the Giant Metre-wave Radio Telescope 1.28 GHz map and a massive protostar candidate, IRS 1, prior to an ultracompact H II phase. Using the Very Large Telescope/NACO near-infrared images, IRS 1 is resolved with a jet-like feature within a 4200 au scale.

Key words: dust, extinction – H II regions – ISM: clouds – ISM: individual objects (IRAS 17599–2148) – stars: formation – stars: pre-main sequence

1. INTRODUCTION

In recent years, *Spitzer* has revealed many massive star-forming (MSF) regions that contain infrared dark clouds (IRDCs), mid-infrared (MIR) shells or bubbles, 6.7 GHz methanol maser emission (MME), H II regions, and young star clusters together. It is indeed obvious that such sites host numerous complex physical processes of star formation. These sites offer the opportunity to explore the key processes that govern the birth and feedback of massive stars ($\gtrsim$8 $M_{\odot}$; e.g., Zinnecker & Yorke 2007; Deharveng et al. 2010; Rathborne et al. 2011; Tackenberg et al. 2012; Tan et al. 2014; Beuther et al. 2015; Dewangan et al. 2015a, 2015b; Ragan et al. 2015; Xu et al. 2016). Furthermore, such regions also help us understand the formation and evolution of stellar clusters. In particular, the understanding of star formation processes demands a multiscale and multiwavelength approach. However, the study of close and large environments of such MSF regions is still lacking, which will help us gain better insight into the ongoing physical processes.

IRAS 17599–2148, situated at a distance of 4.2 kpc (Kim & Koo 2001), has a bipolar appearance at wavelengths longer than 2 μm (Dewangan et al. 2012). The bipolar nebula (BN) was referred to as two mid-IR (MIR) bubbles (CN107 and CN109; Churchwell et al. 2007). An H II region associated with IRAS 17599–2148 (i.e., G8.14+0.23 H II region) is excited by a single star of radio spectral class O6 (Kim & Koo 2001). The 20 cm continuum peak (Dewangan et al. 2012) and a Class II 6.7 GHz MME (peak velocity ∼19.83 km s^{-1}; Szymczak et al. 2012) were reported toward the waist of the BN (see Figure 2 in Dewangan et al. 2012). Using the multiwavelength analysis of the G8.14+0.23 H II region, Dewangan et al. (2012) found noticeable star formation activities on the periphery of the BN and suggested an interaction of the H II region with its surroundings. Simon et al. (2006) reported the IRDC candidates around IRAS 17599–2148 (e.g., G008.25+00.16 and G008.20+00.18), which were identified based on the absorption features against the Galactic background in the 8.3 μm image. The integrated NANTEN ^{12}CO intensity map (beam size ∼2′.6) of the cloud associated with IRAS 17599–2148 was previously reported by Takeuchi et al. (2010), which was referred to as M008.2+0.2 ($V_{\rm lsr}$ ∼ 19 km s^{-1}; a velocity range ∼12–25 km s^{-1}) in their work (see Figure 14(b) in Takeuchi et al. 2010). Based on the ^{12}CO gas distribution, the IRDC candidates traced in the 8.3 μm image are found to be physically linked to the molecular cloud M008.2+0.2 (see Figure 15 in Takeuchi et al. 2010). However, an investigation of star formation activity in these IRDCs is not yet carried out. Shirley et al. (2013) reported the spectroscopic HCO^+ (3–2) line observations toward the 1.1 mm dust continuum sources in the IRAS 17599–2148 region, and some of them are found toward the IRDCs and the BN. These dust continuum sources are traced in a velocity range of 18–21 km s^{-1}, which is in agreement with the velocity of ionized gas (i.e., 20.3 km s^{-1}; Kim & Koo 2001). The knowledge of velocities of ionized gas, MME, and molecular gas confirms the physical association of the IRDC, MME, and BN with the H II region linked to IRAS 17599–2148. Previous studies convincingly suggested that all these sources (i.e., H II region, IRDC, MME, and BN) appear to be located in the same

complex. Despite the availability of numerous observational data sets, the understanding of close (below 10,000 au) and large (more than 10 pc) environments around the IRAS 17599–2148 region is still lacking. The ongoing physical processes around IRAS 17599–2148 have not been systematically examined. In order to understand the physical environment and star formation processes around IRAS 17599–2148, we use the multiwavelength data covering from the near-IR (NIR) to radio wavelengths, which include the ESO Very Large Telescope (VLT) archival adaptive optics NIR images and the Giant Metre-wave Radio Telescope (GMRT) radio continuum high-resolution maps at 0.61 and 1.28 GHz. The ESO-VLT NIR images are employed to probe the inner circumstellar environment of the infrared counterpart(s) (IRc) of exciting source(s) of the H II region and the 6.7 GHz MME. Our analysis is also focused on inferring the distribution of dust temperature, column density, extinction, ionized emission, kinematics of molecular gas, and young stellar objects (YSOs). All together, such analysis helps us characterize in depth the small- and large-scale environments around IRAS 17599–2148, which will allow us to understand the birth and feedback processes of massive stars, as well as the formation and evolution of stellar clusters.

In Section 2, we provide the details of the multiwavelength data sets used in this paper. In Section 3, we characterize the physical environment of the region around IRAS 17599–2148. Furthermore, we identify the stellar populations around the IRAS 17599–2148 region and infer their clustering. In Section 4, we discuss the possible star formation scenario based on our findings. Finally, in Section 5, we provide a summary of conclusions.

2. DATA AND ANALYSIS

Multiscale and multiwavelength data have been used to explore the physical environments around IRAS 17599–2148. In this paper, we selected a region of $\sim 20\farcm8 \times 13\farcm2$ ($\sim$25.4 pc $\times$ 16.1 pc at a distance of 4.2 kpc), centered at $\alpha_{2000} = 18^{h}02^{m}54\fs5$, $\delta_{2000} = -21°46'33\farcs6$.

2.1. New Observations

2.1.1. Radio Continuum Observations

Radio continuum observations of IRAS 17599–2148 at 0.61 and 1.28 GHz bands were obtained using the GMRT on 2012 December 29 and 2012 December 23 (Proposal Code: 23_054; PI: L. K. Dewangan), respectively. The radio data reduction was performed using the AIPS software, following a similar method to that described in Mallick et al. (2012, 2013). The 0.61 and 1.28 GHz maps have rms noise of 0.34 and 0.38 mJy beam^{-1}, respectively. The synthesized beam sizes of the final 0.61 and 1.28 GHz maps are $\sim 5\farcs6 \times 5\farcs2$ and $\sim 2\farcs8 \times 2\farcs4$, respectively.

Note that a large amount of emission from the Galactic plane was expected during the observations, which influences the low-frequency observations and increases the effective antenna temperature. Since IRAS 17599–2148 is located in the Galactic plane, our GMRT 0.61 and 1.28 GHz maps are corrected for system temperature (see Omar et al. 2002; Mallick et al. 2012, 2013; Baug et al. 2015). The details about the adopted procedure of system temperature corrections are described in Mallick et al. (2012, 2013).

2.2. Archival Data

We also obtained publicly available observational data sets from various Galactic plane surveys.

A brief description of these data sets is given below.

2.3. NIR Images

2.3.1. Adaptive Optics NIR Images

The imaging observations of IRAS 17599–2148 were taken with the 8.2 m VLT with the NAOS-CONICA (NACO) adaptive optics system (Lenzen et al. 2003; Rousset et al. 2003) in H band ($\lambda_c = 1.66\,\mu$m, $\Delta\lambda = 0.33\,\mu$m), K_s band ($\lambda_c = 2.18\,\mu$m, $\Delta\lambda = 0.35\,\mu$m), and L' band ($\lambda_c = 3.80\,\mu$m, $\Delta\lambda = 0.62\,\mu$m). We downloaded these data from the ESO-Science Archive Facility (ESO proposal ID: 089.C-0455(A); PI: João Alves). The single-frame exposure time was 21 s in L' band and 24 s in H and K_s bands. We used five H frames, five K_s frames, and 11 L' frames. In each band, the final NACO image was obtained through a standard analysis procedure such as sky subtraction, image registration, combining with the median method, and astrometric calibration, using IRAF and STAR-LINK software. The astrometric calibration of the NACO images was done using the UKIRT NIR Galactic Plane Survey (GPS; Lawrence et al. 2007) K-band point sources. The VLT/NACO H, K_s, and L' images have resolutions of $0\farcs2$ ($\sim$840 au), $0\farcs2$ ($\sim$840 au), and $0\farcs1$ ($\sim$420 au), respectively.

2.3.2. UKIDSS GPS NIR Data

Deep NIR photometric JHK magnitudes of point sources have been retrieved from the UKIDSS GPS sixth archival data release (UKIDSSDR6plus). The UKIDSS observations (resolution $\sim 0\farcs8$) were carried out using the UKIRT Wide Field Camera (Casali et al. 2007). The UKIDSS GPS photometric data were calibrated using the Two Micron All Sky Survey (2MASS; Skrutskie et al. 2006) data. We extracted only reliable NIR photometric data, following the recommendations given in Lucas et al. (2008) and Dewangan et al. (2015a). To avoid saturation, the sources were obtained fainter than $J = 12.1$ mag, $H = 11.1$ mag, and $K = 10.0$ mag in our selected GPS catalog. Furthermore, the 2MASS photometric magnitudes were retrieved for bright sources that were saturated in the GPS catalog.

2.4. Spitzer Data

Photometric images and magnitudes of point sources have been obtained from the *Spitzer* Galactic Legacy Infrared Mid-Plane Survey Extraordinaire (GLIMPSE; Benjamin et al. 2003) survey at 3.6–8.0 μm (resolution $\sim 2''$). The photometric magnitudes were extracted from the GLIMPSE-I Spring '07 highly reliable catalog. Additionally, we also obtained photometry of point sources from Dewangan et al. (2012) near the BN, which are not listed in the GLIMPSE catalog (see Dewangan et al. 2012). The MIPS Inner Galactic Plane Survey (MIPSGAL; Carey et al. 2005) 24 μm data have been utilized in this paper. The MIPSGAL 24 μm photometry has also been obtained from Gutermuth & Heyer (2015). We also performed aperture photometry in the MIPSGAL 24 μm image to extract point sources, which are not listed in the MIPSGAL 24 μm catalog. The photometry was extracted using a $7''$ aperture radius and a sky annulus from $7''$ to $13''$ in IRAF (e.g.,

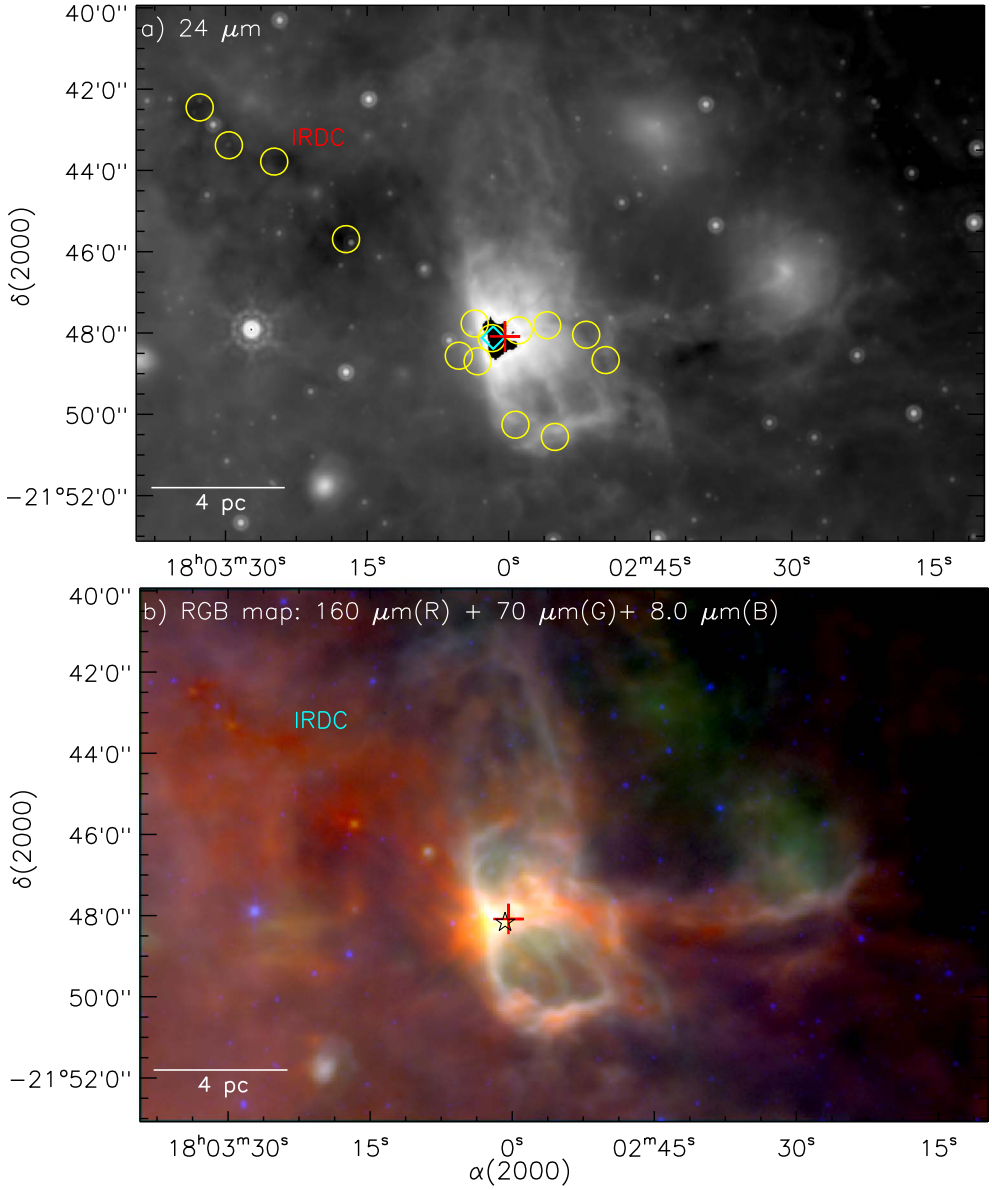

Figure 1. Distribution of the MIR and FIR emission toward the region around IRAS 17599–2148 (size of the selected region $\sim 20'.8 \times 13'.2$ [$\sim$25.4 pc $\times$ 16.1 pc at a distance of 4.2 kpc]; centered at $\alpha_{2000} = 18^h02^m54^s.5$, $\delta_{2000} = -21°46'33''.6$). (a) The MIPSGAL 24 μm image of the region probed in this paper. A diamond symbol shows the VLA 6 cm (5 GHz) radio detection (Becker et al. 1994). The 24 μm image is saturated near the radio detection. The ATLASGAL clumps at 870 μm (Contreras et al. 2013) are also marked by yellow circles. (b) The image is the result of the combination of three bands: 160 μm (red), 70 μm (green), and 8.0 μm (blue). A star symbol indicates the position of the 6.7 GHz MME. In both panels, the position of IRAS 17599–2148 (plus sign) is marked. The scale bar corresponding to 4 pc (at a distance of 4.2 kpc) is shown in both panels. The images have revealed an IRDC (Simon et al. 2006) and a BN (Dewangan et al. 2012).

Dewangan et al. 2015a). The MIPS zero-magnitude flux density, including aperture correction, was adopted for the photometric calibration, as listed in the MIPS Instrument Handbook-Ver-3.

2.5. Herschel, ATLASGAL, and SCUBA-2 Data

Far-IR (FIR) and submillimeter data adopted in this work have been retrieved from the *Herschel Space Observatory* data archives. The processed level2_5 images at 70, 160, 250, 350, and 500 μm were obtained using the *Herschel* Interactive Processing Environment (HIPE; Ott 2010). The beam sizes of these images are $5''.8$, $12''$, $18''$, $25''$, and $37''$ (Griffin et al. 2010; Poglitsch et al. 2010), respectively.

The Submillimetre Common-User Bolometer Array 2 (SCUBA-2) continuum map at 850 μm (beam size $\sim 14''$) was obtained from the James Clerk Maxwell Telescope (JCMT) science archive. In our selected region, we also obtained the positions of 14 dust clumps at 870 μm (Contreras et al. 2013) from the APEX Telescope Large Area Survey of the Galaxy (ATLASGAL; beam size $\sim 19''.2$; Schuller et al. 2009).

2.6. CO (J = 3–2) Line Data

The JCMT HARP CO (3–2) processed data cube was downloaded, and the spatial resolution of the data cube is $16''$. The CO observations were observed on 2009 June 11. The data have a typical rms sensitivity (1σ) of $\approx$0.3 K.

3. RESULTS

3.1. Large-Scale Environment around IRAS 17599–2148

The distribution of molecular gas, dense materials, and ionized emission enables us to infer the physical environment present in and around the IRAS 17599–2148 region.

3.1.1. Infrared and Molecular Emission

On a larger scale, an IRDC and a BN, associated with the bright extended emission, are visually observed in the MIPSGAL 24 μm image (see Figure 1(a)). In the MIPSGAL 24 μm image, the embedded stellar sources are also seen toward the IRDC. Fourteen ATLASGAL dust continuum sources at 870 μm are also marked in Figure 1(a). The ATLASGAL sources are found toward the IRDC and the BN, tracing cold and dense regions. It appears as a chain of dense clumps/cores in our selected target region (e.g., Tafalla & Hacar 2015). In Figure 1(a), the 24 μm image is saturated near the *IRAS* position, where the radio continuum peak position was reported (Becker et al. 1994; Dewangan et al. 2012). Figure 1(b) shows a three-color composite image made using *Herschel* 160 μm in red, *Herschel* 70 μm in green, and GLIMPSE 8.0 μm in blue. The IRDC appears as bright emission regions at wavelengths longer than 24 μm. The BN is also seen as the brightest extended emission in Figure 1(b). Figure 2(a) shows the ATLASGAL and *Herschel* submillimeter images of the region, which trace the cold dust emission (see Section 3.2 for quantitative estimate). The BN is traced in all the *Herschel* images. Interestingly, we infer an elongated filamentary morphology (extension ~21 pc) in the ATLASGAL and *Herschel* submillimeter images, where several condensations are found. Furthermore, the IRDC and the G8.14+0.23 H II region (including the BN) are part of the filamentary structure (see a dashed curve in Figure 2(a)), which is embedded in the cloud associated with IRAS 17599–2148 (i.e., M008.2+0.2; see Figures 14(b) and 15 in Takeuchi et al. 2010). The integrated NANTEN ^{12}CO intensity map (beam size ~2.′6) traces a continuous velocity structure in the direction of IRAS 17599–2148 (Takeuchi et al. 2010). It includes the eastern and western sides of the bubble, as well as the bubble itself (i.e., entire elongated filamentary structure [EFS]; see Figure 14(b) in Takeuchi et al. 2010). Hence, these previous molecular line data, even with coarse beam size, further confirm the existence of the EFS. In Figure 2(a), the *Herschel* images trace the faint dust emission (or infrared bridges) between the ATLASGAL dust continuum sources, which are located within the EFS. Taken together, the submillimeter images and the previously published CO line data reveal the existence of a single EFS in the region probed in this paper.

In Figure 2(b), we present the JCMT CO(J = 3–2) gas emission in the direction of the *IRAS* position. Note that we do not have JCMT molecular line observations for the entire field of view, which is probed in this paper. The JCMT CO data are available only toward the BN. Considering the better resolution of the JCMT HARP CO(3–2) data compared to the previously published NANTEN ^{12}CO data, we are able to observe the bipolar morphology in the integrated JCMT CO intensity map (in a velocity range of 14–26 km s^{-1}). The kinematics of molecular gas are described in Section 3.3. In Figure 2(b), the 850 μm continuum emission, which traces the densest materials, is also overlaid on the integrated CO map and is

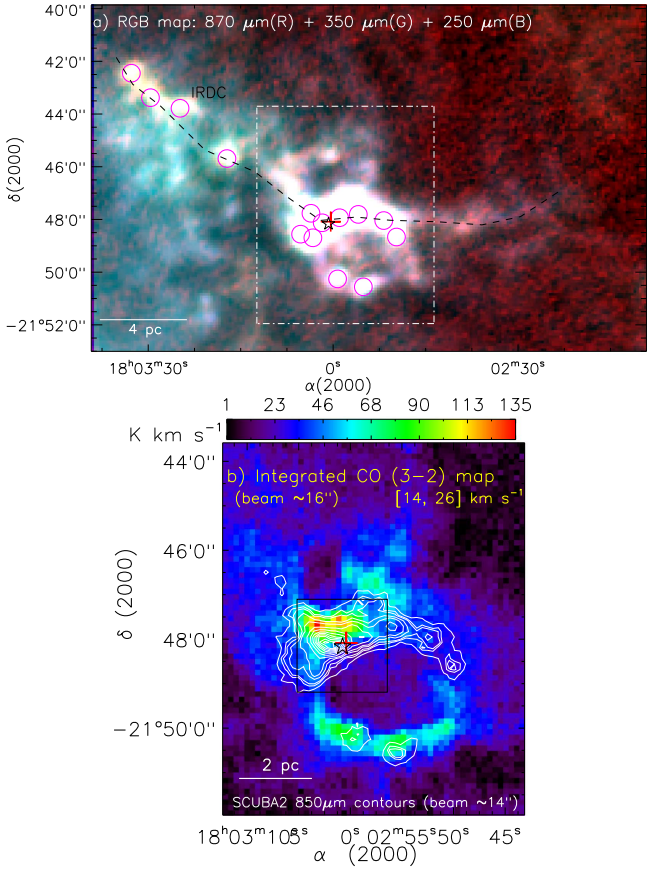

Figure 2. (a) Three-color composite image (*red*, ATLASGAL 870 μm; *green*, *Herschel* 350 μm; *blue*, *Herschel* 250 μm; in linear scale) of the region around IRAS 17599–2148, which clearly traces the cold dust emission. An EFS is highlighted by a dashed curve. The ATLASGAL clumps at 870 μm (Contreras et al. 2013) are also marked by magenta circles. The faint dust emissions (or infrared bridges) traced in the *Herschel* images are also found between the ATLASGAL clumps, indicating that this chain of dense clumps/cores belongs to a single entity (i.e., EFS; see the dashed curve) (also see text for details). The dot-dashed white box encompasses the area shown in panel (b). The scale bar at the bottom left corner corresponds to 4 pc (at a distance of 4.2 kpc). (b) Integrated CO (3–2) emission map overlaid with the SCUBA-2 850 μm contours. The 850 μm contours are superimposed with levels of 4%, 8%, 10%, 15%, 20%, 30%, 40%, 50%, 60%, 70%, 80%, 90%, and 97% of the peak value (i.e., 15.5 mJy arcsec^{-2}). The figure shows the distribution of molecular gas and dense materials in the region around IRAS 17599–2148. The solid black box encompasses the area shown in Figure 3. The scale bar at the bottom left corner corresponds to 2 pc (at a distance of 4.2 kpc). In both panels, the marked symbols are similar to those shown in Figure 1.

mostly distributed toward the waist of the BN. The 850 μm continuum map (beam size ~14″) reveals two peaks (i.e., dense clumps/cores), and one of them coincides with a Class II 6.7 GHz MME. The 6.7 GHz MME is a reliable tracer of massive young stellar objects (MYSOs; e.g., Walsh et al. 1998; Minier et al. 2001; Urquhart et al. 2013).

3.1.2. Radio Continuum Emission

In order to trace the distribution of ionized emission, we present high-resolution GMRT radio continuum maps at 0.61 GHz (beam size ~5.″6 × 5.″2) and 1.28 GHz (beam size ~2.″8 × 2.″4) of the region around IRAS 17599–2148. Figure 3 shows the GMRT 0.61 GHz (top panel) and 1.28 GHz (bottom panel) contours overlaid on the *Spitzer* 4.5 μm image. Note that the radio emission is not detected toward the IRDC (not shown here) and is found only toward the previously known G8.14

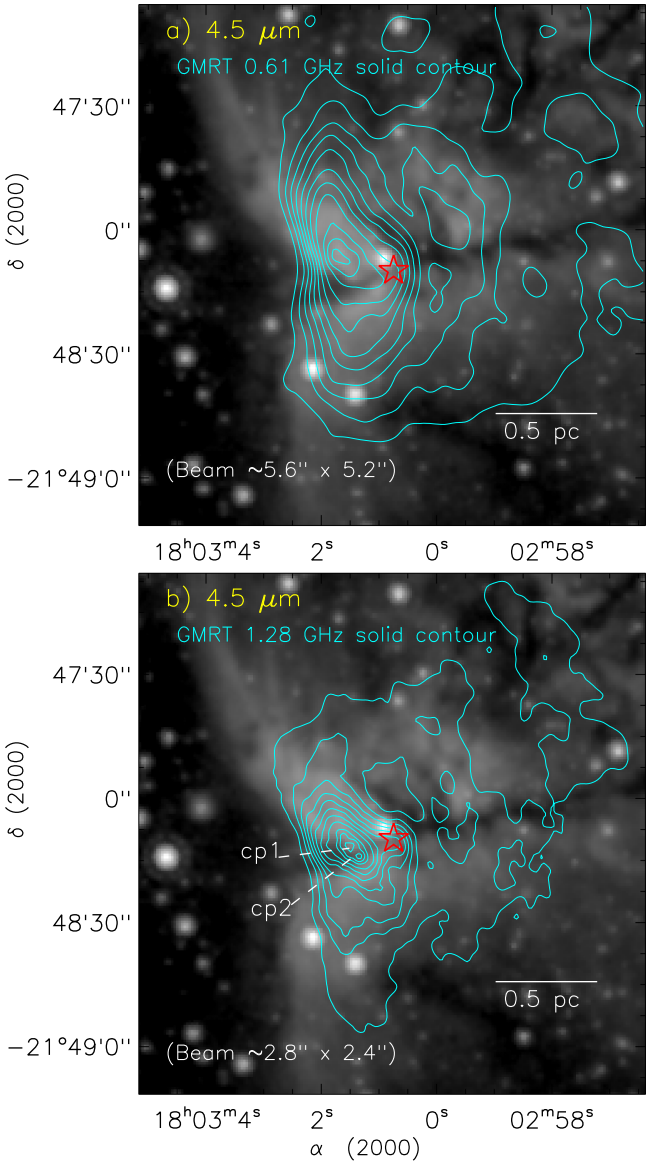

Figure 3. High-resolution GMRT radio continuum emissions at (a) 0.61 GHz (beam size ~5.″6 × 5.″2) and (b) 1.28 GHz (beam size ~2.″8 × 2.″4). In each panel, the radio contours are overlaid on the 4.5 μm image. The 1.28 GHz map traces two compact peaks (i.e., cp1 and cp2), which are also labeled in panel (b). In both panels, the contours are overlaid with levels of 10%, 20%, 30%, 40%, 50%, 60%, 70%, 80%, 90%, 95%, and 99% of the peak values (i.e., 0.0738 Jy beam^{-1} for 0.61 GHz; 0.0225 Jy beam^{-1} for 1.28 GHz). In both panels, a star symbol indicates the position of the 6.7 GHz MME. In both panels, the scale bar at the bottom right corner corresponds to 0.5 pc (at a distance of 4.2 kpc).

+0.23 H II region. However, these new maps provide more insight into the radio peak, due to the high-resolution map, compared to the previously reported radio continuum map at 20 cm (beam ~6″; Dewangan et al. 2012). Both GMRT maps show similar morphology of the ionized emission, and their peak positions are offset from the 6.7 GHz MME. The extended morphology and a single peak at 0.61 GHz map are similar to what was previously seen in the 20 cm map (Dewangan et al. 2012). In addition to the extended morphology, due to high-resolution observations, the 1.28 GHz map has resolved a single peak (as seen in the 0.61 GHz map) into two compact peaks (see Figure 3(b)) (i.e., cp1 [α_{2000} = 18^{h}03^{m}01.^{s}49, δ_{2000} = −21°48′12.″23; peak flux density = 22.52 mJy/beam; angular size = 28.″78 × 13.″95; deconvolved size = 28.″66 × 13.″71] and cp2 [α_{2000} = 18^{h}03^{m}01.^{s}38, δ_{2000} = −21°48′13.″82; peak flux density = 22.63 mJy/beam; angular size = 14.″25 × 9.″93; deconvolved size = 14.″02 × 9.″57]). Using the 1.28 GHz map, we computed the integrated flux densities equal to 1355.50 and 480.12 mJy for the cp1 and cp2 peaks, respectively. These integrated flux densities are utilized to compute the number of Lyman continuum photons ($N_{\rm uv}$). The equation of $N_{\rm uv}$ is given by (Matsakis et al. 1976),

$$N_{uv}(s^{-1}) = 7.5 \times 10^{46}\left(\frac{S_\nu}{\rm Jy}\right)\left(\frac{D}{\rm kpc}\right)^2\left(\frac{T_e}{10^4\ {\rm K}}\right)^{-0.45} \times \left(\frac{\nu}{\rm GHz}\right)^{0.1}, \quad (1)$$

where S_ν is the measured total flux density in Jy, D is the distance in kpc, T_e is the electron temperature, and ν is the frequency in GHz. The analysis is done for a distance of 4.2 kpc and for an electron temperature of 10,000 K. We find $N_{\rm uv}$ (or $\log N_{\rm uv}$) to be ~1.86 × 10^{48} s^{-1} (48.27) and ~6.6 × 10^{47} s^{-1} (47.82) for cp1 and cp2, respectively. These estimates correspond to a single ionizing star of spectral type O8V–O8.5V and O9V–O9.5V (see Table 1 in Martins et al. 2005 for theoretical values) for cp1 and cp2, respectively. Based on these results, within 18″ of the *IRAS* position, two radio O spectral type sources and a 6.7 GHz MME (without radio peak) are present, indicating the presence of different early evolutionary stages of massive star formation. The search of the driving sources of the radio peaks and the 6.7 GHz MME is presented in Section 3.4.

We also computed the integrated flux densities of the extended radio morphology seen (at 3σ) in both radio maps. Using Equation (1), the estimation of $N_{\rm uv}$ is also performed for both radio frequencies (0.61 and 1.28 GHz) separately. Taking into account D = 4.2 kpc, T_e = 10,000 K, and $S_{1.28}$ = 3.39 Jy, we find $N_{\rm uv}$ (or $\log N_{\rm uv}$) = 4.7 × 10^{48} s^{-1} (48.67). Similarly, we obtain $N_{\rm uv}$ (or $\log N_{\rm uv}$) = 6.9 × 10^{48} s^{-1} (48.84) for D, T_e, and $S_{0.61}$ = 5.39 Jy. The estimates of $N_{\rm uv}$ values at different frequencies correspond to a single ionizing star of O6V–O6.5V spectral type (Martins et al. 2005), which is consistent with the previously reported spectral type of the ionizing source of the G8.14+0.23 H II region (e.g., Kim & Koo 2001).

Within the EFS, the radio emission is detected toward the IRAS 17599–2148 position and is absent toward the IRDC, revealing different evolutionary stages of star formation.

3.2. Herschel Temperature and Column Density Maps

In recent years, the *Herschel* temperature and column density maps have been very useful tools for studying the distribution of column density, temperature, extinction, and clump mass in a given star-forming region. In this section, we also present these maps of the selected region around IRAS 17599–2148. We produced the temperature and column density maps of the region, in a manner similar to that described in Mallick et al. (2015) (also see Dewangan et al. 2015a). Here, we also give a brief step-by-step description of the procedures.

The *Herschel* temperature and column density maps are obtained from a pixel-by-pixel spectral energy distribution (SED) fit with a modified blackbody to the cold dust emission in the *Herschel* 160–500 μm wavelengths. The *Herschel* 70 μm

data are not included in the analysis, because the 70 μm emission is dominated by UV-heated warm dust. The *Herschel* image at 160 μm is in units of Jy pixel^{-1}, and the images at 250–500 μm are calibrated in the surface brightness units of MJy sr^{-1}. The plate scales of the 160, 250, 350, and 500 μm images are 3.″2, 6″, 10″, and 14″ pixel^{-1}, respectively. Before the SED fit, all images were convolved to the angular resolution of the 500 μm image ($\sim$37″) and were brought to the same flux unit (i.e., Jy pixel^{-1}). Furthermore, the images were regridded to the pixel size of the 500 μm image ($\sim$14″). These procedures were performed using the convolution kernels available in the HIPE software. Next, the sky background flux level was determined to be 0.393, 1.125, 2.528, and $-$0.186 Jy pixel^{-1} for the 500, 350, 250, and 160 μm images (size of the selected region $\sim$7.′7 $\times$ 8.′2; centered at α_{J2000} = 18^{h}03^{m}41^s, δ_{J2000} = $-$20°52′49.″6), respectively. The featureless dark area away from the selected target region, to avoid diffuse emission associated with the target, was carefully selected for the background estimation.

In the final step, a modified blackbody was fitted to the observed fluxes on a pixel-by-pixel basis, in order to obtain the maps (see Equations (8) and (9) given in Mallick et al. 2015). The fitting was performed using the four data points for each pixel, retaining the dust temperature (T_d) and the column density (N(H$_2$)) as free parameters. In the calculations, we utilized a mean molecular weight per hydrogen molecule μ_{H2} = 2.8 (Kauffmann et al. 2008) and an absorption coefficient $\kappa_\nu = 0.1(\nu/1000\,\mathrm{GHz})^\beta\,\mathrm{cm^2\,g^{-1}}$, including a gas-to-dust ratio R_t = 100, with a dust spectral index of β = 2 (see Hildebrand 1983). The final temperature and column density maps (resolution $\sim$37″) are shown in Figure 4.

The *Herschel* temperature map traces the IRDC in a temperature range of about 16–22 K, while the considerably warmer gas ($T_d \sim$ 25–39 K) is found toward the *IRAS* position (including the H II region and the BN; see Figure 4(a)). This implies that the cold gas is exclusively found toward the IRDC, while the warmer gas is detected toward the H II region. In Figure 4(b), the IRDC and the BN are traced with higher column densities. Several condensations are seen in the column density map (see Figure 4(b)). The condensation having the highest column density (peak $N(H_2) \sim 1.1 \times 10^{23}\,\mathrm{cm^{-2}}$; $A_V \sim$ 117 mag) is associated with the H II region and the 6.7 GHz MME. The relation between optical extinction and hydrogen column density ($A_V = 1.07 \times 10^{-21}\,N(H_2)$; Bohlin et al. 1978) is adopted here.

3.2.1. Herschel Clumps

In the column density map, the *clumpfind* algorithm (Williams et al. 1994) has been applied to identify the clumps and their total column densities. Twelve clumps are identified, which are labeled in Figure 4(b), and their boundaries are also shown in Figure 4(c). We estimated the masses of these clumps using their total column densities. The mass of a single clump can be computed using the formula,

$$M_{\rm clump} = \mu_{\rm H_2}\, m_H\, {\rm Area_{pix}} \Sigma N\,(H_2), \qquad (2)$$

where $\mu_{\rm H_2}$ is assumed to be 2.8, Area$_{\rm pix}$ is the area subtended by 1 pixel, and ΣN(H$_2$) is the total column density. The mass of each *Herschel* clump is listed in Table 1. The table also contains an effective radius of each clump, which is provided by the *clumpfind* algorithm. The clump masses vary between

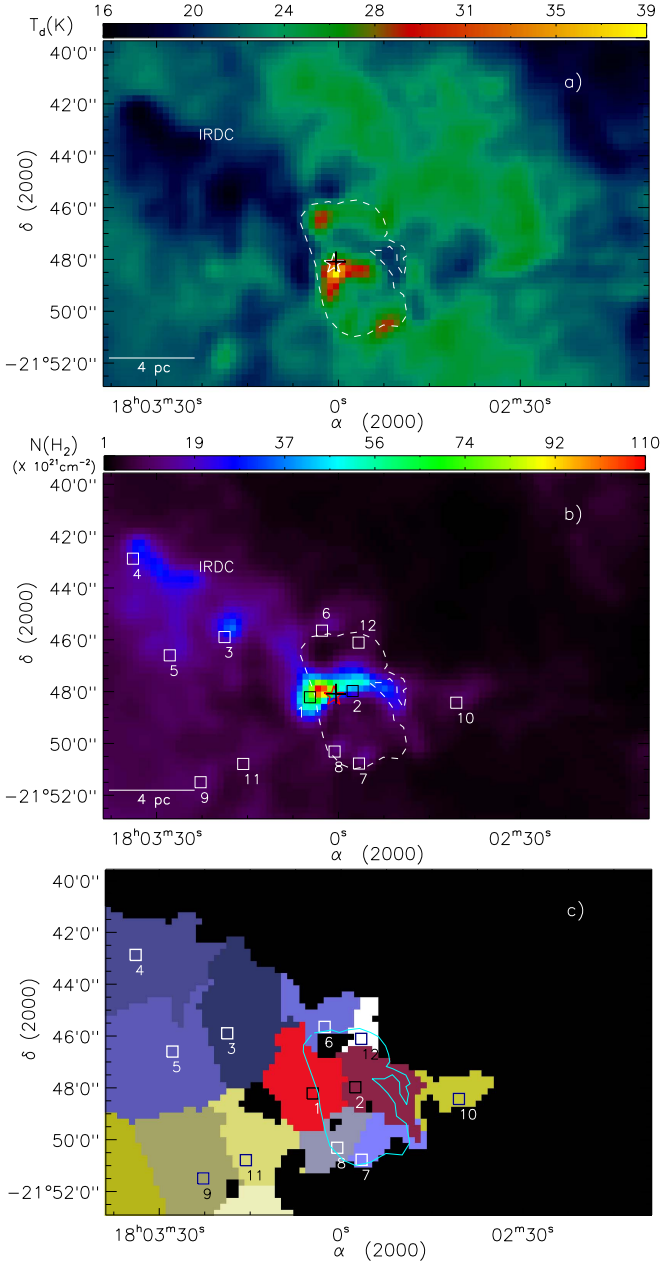

Figure 4. *Herschel* (a) temperature map and (b) column density (N(H$_2$)) map of the region around IRAS 17599–2148 (see text for details). The column density map allows us to infer the extinction with $A_V = 1.07 \times 10^{-21} N(H_2)$ and to identify the clumps (see text for details). The identified clumps are marked by squares, and the boundaries of these clumps are shown in panel (c) (also see Table 1). (c) The boundary of each identified clump is highlighted along with its corresponding clump ID (see Table 1 and also panel (b)). A BN is depicted from the *Spitzer* 8 μm emission (see Dewangan et al. 2012), which is shown in all the panels. In the first two panels, the other marked symbols are similar to those shown in Figure 1. In the first two panels, the scale bar at the bottom right corner corresponds to 4 pc (at a distance of 4.2 kpc).

410 and 7024 $M_\odot$. The EFS is associated with at least six massive clumps (i.e., IDs 1–5 and 10), indicating the fragmentation of the cloud. The most massive condensation (i.e ID 1) hosts two compact radio continuum sources and the 6.7 GHz MME, which is located at the waist of the BN. At least three massive and cold condensations (i.e., IDs 3–5) are seen toward the IRDC. At least four condensations (i.e., IDs 6–8 and 12) are also found at the edges of the BN.

Table 1
Summary of the Properties of the Identified *Herschel* Clumps within the Region Probed in This Paper Using the *Herschel* Data (see Figures 4(b) and (c))

ID	R.A. [J2000]	Decl. [J2000]	R_c[a] (pc)	$M_{\rm clump}$ ($M_\odot$)	$P_{\rm clump}$ (10^{-10} dynes cm^{-2})	$t_{\rm ff,sph}$ (Myr)	$V_{\rm peak}$ (km s^{-1})	ΔV (km s^{-1})	$M_{\rm vir}$ ($M_\odot$)
1	18:03:04.7	−21:48:13.0	2.0	7023.7	29.2	0.39	18.6[b]	3.36[b]	2830
2	18:02:57.7	−21:47:58.6	1.8	4147.6	14.8	0.47	18.58[b]	3.39[b]	2625
3	18:03:18.8	−21:45:53.6	2.5	5454.5	6.9	0.57	18.7[c]	3.1[c]	3047
4	18:03:33.9	−21:42:52.2	2.5	6418.6	9.6	0.52	18.9[c]	2.7[c]	2306
5	18:03:27.8	−21:46:36.0	2.9	6422	5.5	0.60	⋯	⋯	⋯
6	18:03:02.7	−21:45:38.9	1.4	1192.6	3.6	0.66	⋯	⋯	⋯
7	18:02:56.6	−21:50:46.5	1.2	763.8	3.0	0.70	⋯	⋯	⋯
8	18:03:00.6	−21:50:18.7	1.4	1046.2	2.8	0.70	⋯	⋯	⋯
9	18:03:22.7	−21:51:29.7	2.4	3377.9	3.3	0.70	⋯	⋯	⋯
10	18:02:40.6	−21:48:25.7	1.2	776.8	2.3	0.74	⋯	⋯	⋯
11	18:03:15.7	−21:50:47.4	1.8	1678.5	2.5	0.73	⋯	⋯	⋯
12	18:02:56.7	−21:46:06.6	0.9	410	2.1	0.76	⋯	⋯	⋯

Notes. Column (1) lists the IDs given to the clump. The table also contains positions, deconvolved effective radius (R_c), clump mass ($M_{\rm clump}$), self-gravitating pressure ($P_{\rm clump} \approx \pi G\,(M_{\rm clump}/\pi R_c^2)^2$), spherical free-fall time ($t_{\rm ff,sph} \approx 16.6(R_c/{\rm pc})^{3/2}(M_{\rm clump}/M_\odot)^{-1/2}$), peak velocity ($V_{\rm peak}$), line width ($\Delta V$), and virial mass ($M_{\rm vir} = 126R_c\Delta V^2$).
[a] Estimated using the *clumpfind* algorithm.
[b] $NH_3(1, 1)$ derived line parameters from Wienen et al. (2012).
[c] $HCO^+(3–2)$ derived line parameters from Shirley et al. (2013).

In order to examine the internal dynamical properties of these clumps in more detail, we computed their physical parameters (such as spherical free-fall time, virial mass, virial parameter, self-gravitating pressure, and Mach number). Using the mass ($M_{\rm clump}$) and radius (R_c) of each clump, we can estimate the mean mass density ρ_0 and the spherical free-fall time $t_{\rm ff,sph} = (3\pi/32G\rho_0)^{1/2}$ $(=16.6\ (R_c/{\rm pc})^{3/2}\ (M_{\rm clump}/M_\odot)^{-1/2}$ Myr). We estimated $t_{\rm ff,sph}$ values for our identified clumps ranging from 0.4 to 0.77 Myr, which are tabulated in Table 1.

In each clump, the pressure exerted by the self-gravity of the molecular gas can be estimated using $P_{\rm clump} \approx \pi G\,(M_{\rm clump}/\pi R_c^2)^2$. The value of $P_{\rm clump}$ is tabulated in Table 1. In general, the pressure associated with a typical cool molecular cloud ($P_{\rm MC}$) is found to be $\sim 10^{-11}$–10^{-12} dynes cm^{-2} (for a temperature of ∼20 K and a particle density of $\sim 10^3$–10^4 cm^{-3}) (see Table 7.3 of Dyson & Williams 1980, p. 204), which is much lower than $P_{\rm clump}$. This comparison indicates an acting of self-gravity and a signature of star formation activity in these clumps.

To infer whether the identified clumps are stable or unstable against gravitational collapse, the virial mass analysis is employed. As mentioned above, we find six clumps associated with the filamentary structure, and two of them are located at the waist of the BN. The molecular line observations were reported toward four out of these six clumps. We estimated virial mass ($M_{\rm vir}$) and virial parameter ($M_{\rm vir}/M_{\rm clump}$) for these four clumps where line width values were measured. The virial mass of a clump of radius R_c (in pc) and line width ΔV (in km s^{-1}) is defined as $M_{\rm vir}\ (M_\odot) = kR_c\Delta V^2$ (MacLaren et al. 1988), where the geometrical parameter $k = 126$ for a density profile $\rho \propto 1/r^2$. A virial parameter less than 1 suggests a clump prone to collapse, and greater than 1 suggests one resistant to collapse. For these clumps, the virial parameter is less than 1, indicating unstable clumps against gravitational collapse.

Following Dewangan et al. (2016), we estimated thermal sound speed (a_s) and nonthermal velocity dispersion ($\sigma_{\rm NT}$) of the two clumps where gas kinetic temperature ($T_{\rm kin}$) values were reported (Wienen et al. 2012). Wienen et al. (2012) estimated $T_{\rm kin}$ for clumps 1 and 2 to be 22.86 and 17.71 K, respectively. The sound speed a_s $(=(kT_{\rm kin}/\mu m_H)^{1/2})$ is computed using $T_{\rm kin}$ and $\mu = 2.37$ (approximately 70% H and 28% He by mass). The nonthermal velocity dispersion is defined by

$$\sigma_{\rm NT} = \sqrt{\frac{\Delta V^2}{8\ln 2} - \frac{kT_{\rm kin}}{17m_H}} = \sqrt{\frac{\Delta V^2}{8\ln 2} - \sigma_{\rm T}^2}, \quad (3)$$

where ΔV is the measured line width of the observed NH_3 spectra, $\sigma_{\rm T}$ $(=(kT_{\rm kin}/17m_H)^{1/2})$ is the thermal broadening for NH_3 at $T_{\rm kin}$ (e.g., Dunham et al. 2011), and m_H is the mass of the hydrogen atom. We obtain a_s and $\sigma_{\rm NT}$ to be 0.28 and 1.42 for clump 1, respectively, while $a_s = 0.25$ and $\sigma_{\rm NT} = 1.44$ for clump 2, respectively. These values give us Mach numbers ($\sigma_{\rm NT}/a_s$) of 5 and 5.8 for clumps 1 and 2, respectively, indicating that these clumps are supersonic where nonthermal motions are dominated. The nonthermal motions could be explained by turbulence and outflows from YSOs.

3.3. Velocity Field

Previously, Dewangan et al. (2012) studied the G8.14+0.23 H II region and suggested the possibility of triggered star formation by the expansion of this H II region. In order to further examine the expansion of the H II region, we present a kinematic analysis of the molecular gas in the G8.14+0.23 H II region. In Figure 5, the integrated CO intensity map and the position–velocity diagrams are presented. The position–velocity diagrams of the CO emission are shown with different position angles, tracing a C-like and a ring-like structure. Recently, Arce et al. (2011) studied the molecular gas distribution in the Perseus molecular cloud and compared a model of expanding bubbles in a turbulent medium. These authors predicted a C-like or ring-like structure for an expanding shell/bubble in the position–velocity diagrams (see Figure 5 in Arce et al. 2011). In this work, the radio continuum maps suggest that the H II region associated with IRAS 17599–2148 can be excited by a single source of radio

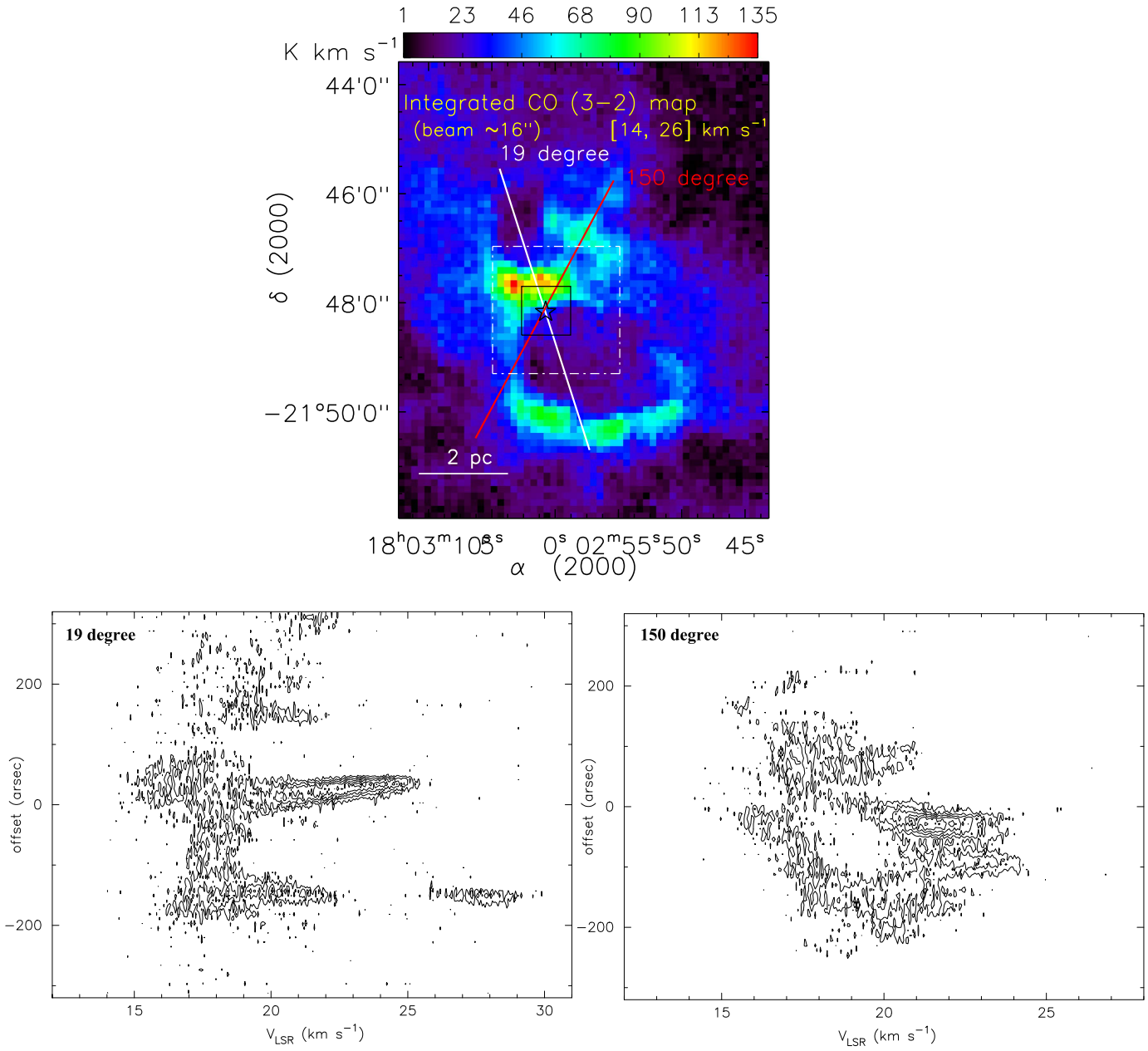

Figure 5. Top panel: integrated CO (3–2) emission map of the region around IRAS 17599–2148, similar to that shown in Figure 2(b). The two solid lines with different position angles represent the axes, where the position–velocity diagrams are extracted. A star symbol indicates the position of the 6.7 GHz MME. The scale bar at the bottom left corner corresponds to 2 pc (at a distance of 4.2 kpc). The dot-dashed white box is shown as a zoomed-in view in Figure 6(a). The solid black box is shown as a zoomed-in view in Figure 8(a). Bottom left: position–velocity diagram along the axis with a position angle of 19° (see top panel in Figure 5). Bottom right: position–velocity diagram along the axis with a position angle of 150° (see top panel in Figure 5). In the two bottom panels, the offset reference is the position of the 6.7 GHz MME. The position–velocity diagrams show a C-like and a ring-like structure of gas, indicating the expanding shell with an expanding gas velocity of ~4.5 km s^{-1}.

spectral type O6V–O6.5V. Hence, the structures seen in the position–velocity diagrams can be explained by the expanding H II region with an expansion velocity of the gas of ~4.5 km s^{-1}.

Furthermore, the position–velocity diagrams show a noticeable velocity gradient toward the IRAS 17599–2148 region, indicating the presence of a molecular outflow(s). Due to the coarse beam of CO (3–2) line data, it is indeed a difficult task to explore the real driver(s) of the outflow(s). Figure 6(a) shows the distribution of ionized and dust continuum emissions. It seems that the exciting source of the outflow could be the driving source of the H II region or of the 6.7 GHz MME. Hence, high-resolution molecular line observations will be required to further explore the outflow activity in the IRAS 17599–2148 region.

Due to the lack of JCMT molecular line observations toward the IRDC, the analysis presented in this work does not provide any information on the molecular gas kinematics toward the IRDC.

3.4. Small-scale Environment toward IRAS 17599–2148

In order to explore the driving source(s) of the 6.7 GHz MME and the radio continuum peaks, we examined the UKIDSS GPS and GLIMPSE images toward the IRAS

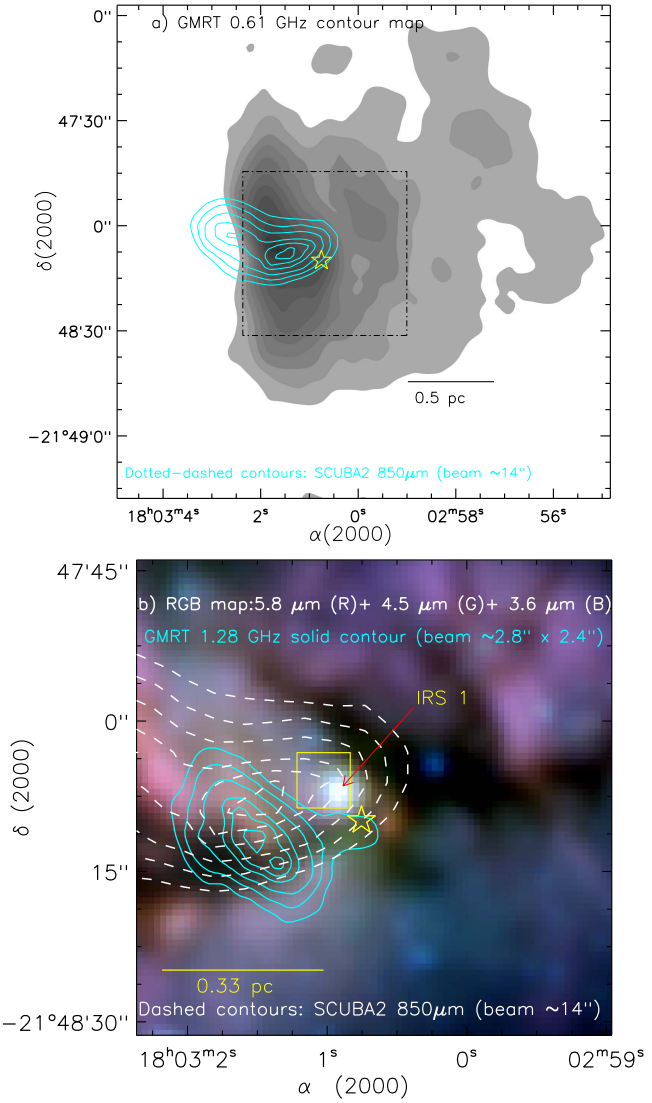

Figure 6. (a) Radio continuum contour map at 0.61 GHz is overplotted with contours of 850 μm emission (see dot-dashed contours). The 0.61 GHz contours are shown with similar levels to those shown in Figure 3(a). The dot-dashed black box encompasses the area shown in Figure 6(b). The scale bar at the bottom right corner corresponds to 0.5 pc (at a distance of 4.2 kpc). The figure shows the distribution of ionized and dust continuum emissions. (b) Three-color composite image (*red*, 5.8 μm; *green*, 4.5 μm; *blue*, 3.6 μm; in log scale) of the region around IRS 1. The 1.28 GHz emission is also overlaid by contours with levels of 60%, 70%, 80%, 90%, 95%, and 99% of the peak value (i.e., 0.0225 Jy beam^{-1}). IRS 1, previously reported by Dewangan et al. (2012), appears to be the reddest and brightest in the *Spitzer* images and is located close to the submillimeter emission peak, as well as the Class II 6.7 GHz MME position. The solid yellow box is shown as a zoomed-in view in Figures 7(a)–(c). The scale bar at the bottom left corner corresponds to 0.33 pc (at a distance of 4.2 kpc). In both panels, the 850 μm emission is also overlaid by contours with levels of 60%, 70%, 80%, 90%, 95%, and 99% of the peak value (i.e., 15.5 mJy arcsec^{-2}). In both panels, the position of the 6.7 GHz MME is marked with a star symbol.

17599–2148 position. We also utilized the ESO-VLT NIR images to probe the inner circumstellar environment of the driving sources.

3.4.1. Infrared Counterpart of 6.7 GHz MME

Figure 6(b) shows a three-color composite image made using the GLIMPSE images (5.8 μm in red; 4.5 μm in green; 3.6 μm in blue), which is also overlaid with the 1.28 GHz and 850 μm emission. A point-like source appears the reddest and brightest in the *Spitzer* images and is located very close to the submillimeter emission peak (a projected linear separation of $\sim$8″) and the 6.7 GHz MME (a projected linear separation of $\sim$4″). The source was previously designated as IRS 1 and was characterized as a candidate MYSO (stellar mass $\sim 10 \pm 2\,M_{\odot}$) based on its SED modeling from the NIR to submillimeter data (see Figure 11 in Dewangan et al. 2012). IRS 1 is barely observed in the GPS *H*-band image (not shown here); however, it is seen as a single object in the GPS *K*-band image (resolution $\sim$0.″8; not shown here) and the GLIMPSE 3.6–8.0 μm images (resolution $\sim$2″) (see Figure 6(b)). IRS 1 is an embedded source located very close to the peak of the 6.7 GHz MME and is associated with a clump having the highest column density. Additionally, considering IRS 1 as a single bright source in the GLIMSE images, we consider the IRS 1 source as an infrared counterpart (IRc) of the 6.7 GHz MME. At the sensitivity of the observed GMRT radio map ($3\sigma \sim 1.14$ mJy beam^{-1}), IRS 1 is situated at a projected linear separation of $\sim$10″ from the radio peaks seen in the 1.28 GHz map, which suggests that IRS 1 is not associated with any radio continuum peak (or an ultracompact (UC) H II region; see Figure 6(b)). Hence, IRS 1 cannot be the powering source of the H II region associated with the IRAS 17599–2148 region. As mentioned before, the 6.7 GHz MME is a reliable tracer of MYSOs (e.g., Walsh et al. 1998; Minier et al. 2001; Urquhart et al. 2013). Altogether, IRS 1 could be a genuine massive protostar candidate (mass $\sim 10 \pm 2\,M_{\odot}$) in a very early evolutionary stage, before the onset of a UCH II region. Based on the presence of two compact radio continuum sources (with the radio spectral class of O-type stars) and the MME, the IRAS 17599–2148 region appears to be a very similar system to W42 (see Figure 2 in Dewangan et al. 2015a).

In order to study the small-scale environment of IRS 1, we present the ESO-VLT archival NIR images. In Figure 7, we show the VLT/NACO adaptive optics images of IRS 1 in *H*, K_s, and L' bands. The VLT/NACO *H*-band image detects a faint point-like source, while K_s and L' images resolve the IRS 1 into at least three point-like sources (i.e., designated as IRS 1a, IRS 1b, and IRS 1c; see Figure 7(b)) within a scale of $\sim$4200 au, and one of the sources (i.e., IRS 1a) is associated with the diffuse emission (see Figures 7(b) and (c)). We find these sources in the separation range from $\sim$0.″33 (1390 au) to $\sim$0.″57 (2400 au). De Villiers et al. (2015) summarized that the 6.7 GHz masers switch on after the onset of the outflow. The diffuse emission seen below the $\sim$4200 au scale with IRS 1a might be linked to the outflow. In general, the NIR emission is attributed to scattered light escaping through the outflow cavity (e.g., Zhang & Tan 2011). Hence, the diffuse emission feature could be a jet, which appears as a narrow emission feature and may be located inside an outflow cavity as traced in the L' image. Additionally, Urquhart et al. (2013) suggested the exclusive association of Class II 6.7 GHz methanol masers with MYSOs. Hence, IRS 1a could be the main massive protostar among other point-like sources in the IRS 1 system.

Additionally, the multiplicity of point-like sources has been observed around IRS 1 within a scale of 4200 au. Massive stars are generally found in binary and multiple systems (Duchêne & Kraus 2013). For example, in M8 and W42 star-forming regions, the well-characterized "O" stars are resolved

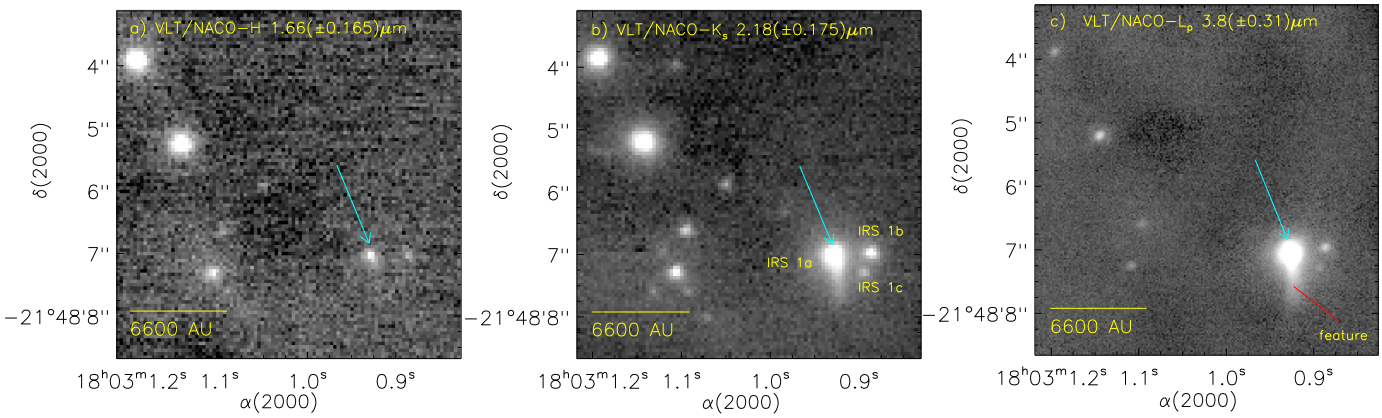

Figure 7. VLT/NACO adaptive optics H, K_s, and L' images of the region around IRS 1 (in log scale). The selected area of the VLT/NACO images is shown by a solid box in Figure 6(b). In each panel, the position of a resolved point-like source ($\alpha_{2000} = 18^h03^m00^s.93$, $\delta_{2000} = -21°48'07''.05$) is highlighted by an arrow. In each panel, the scale bar at the bottom left corner corresponds to 6600 au (at a distance of 4.2 kpc). The NACO images have resolved IRS 1 into at least three point-like sources (labeled as IRS 1a, 1b, and 1c), and one of them is associated with a diffuse emission feature within a scale of 4200 au.

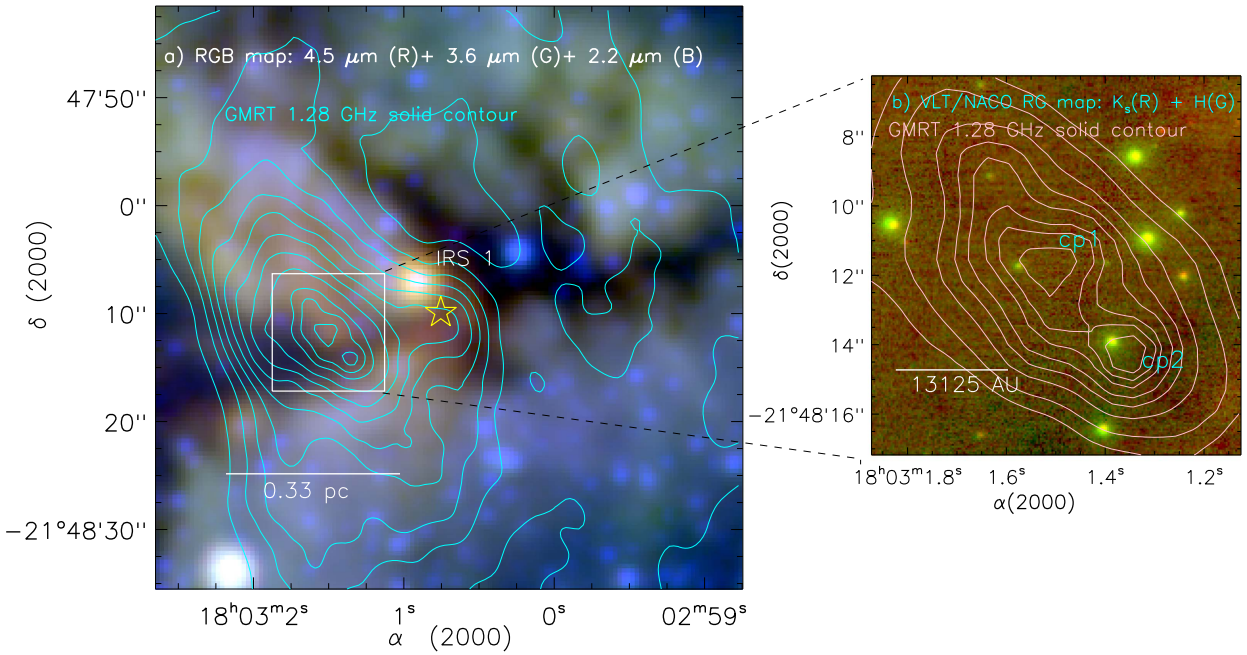

Figure 8. (a) Three-color composite image (*red*, 4.5 μm; *green*, 3.6 μm; *blue*, 2.2 μm; in log scale) of the region around IRS 1. The 1.28 GHz emission is also overlaid by contours with similar levels as shown in Figure 3(b). The solid white box encompasses the area shown in panel (b). A star symbol indicates the position of the 6.7 GHz MME. The scale bar at the bottom left corner corresponds to 0.33 pc (at a distance of 4.2 kpc). (b) The VLT/NACO two-color composite image (*green*, H band; red, K_s band; in log scale) of the region around the radio compact peaks. The selected area of the VLT/NACO images is shown by a box in panel (a), tracing the small-scale environment. The 1.28 GHz radio contours are also overlaid with levels of 80%, 85%, 90%, 93%, 95%, 97%, 98%, and 99% of the peak value (i.e., 0.0225 Jy beam^{-1}). The scale bar at the bottom left corner corresponds to 13,125 au (at a distance of 4.2 kpc). In the VLT/NACO images, a point-like source (without any diffuse emission) is seen toward each radio peak.

into multiple sources using the high-resolution NIR images (Goto et al. 2006; Dewangan et al. 2015a). Around IRS 1, the multiple sources are found in the separation range from $\sim$0$''$.33 (1390 au) to $\sim$0$''$.57 (2400 au). Due to the coarse beam of the JCMT-SCUBA-2, the 850 μm map is unable to resolve the dense core associated with the IRS 1 source. Based on the separation of the sources in the IRS 1 multiple system, the possibility of core fragmentation may explain the origin of multiple systems (see Tobin et al. 2016, and references therein).

Based on these indicative results, further detailed studies of IRS 1 are encouraged using high-resolution interferometric observations at longer wavelength.

3.4.2. Infrared Counterparts of Compact Radio Peaks

To trace the IRcs of two compact radio peaks (cp1 and cp2), Figure 8(a) shows a three-color composite image using 4.5 μm (red), 3.6 μm (green), and 2.2 μm (blue), which is also overlaid with the 1.28 GHz emission. The source seen close to the peak cp1 is barely observed in the GPS K-band image. The source seen close to the peak cp2 is also observed in the GPS K-band image (position and JHK photometry: α_{2000} = 18:03:01.38, δ_{2000} = −21:48:13.96; m_J = 18.22 ± 0.07 mag; m_H = 17.39 ± 0.08 mag; m_K = 17.79 ± 0.3 mag). In Figure 8(b), we present the VLT/NACO adaptive optics NIR images (H and K_s; below the 8000 au scale) toward the radio peaks (i.e., cp1 and cp2). A point-like source is seen toward each compact

radio peak in the VLT/NACO images. There are no nebular features seen toward these sources in the NACO images.

A high-resolution spectroscopic study will be very helpful to confirm the ionizing sources of the radio peaks.

3.5. Young Stellar Objects

3.5.1. Study of Identification of YSOs

The study of YSO populations is a powerful tool to depict the picture of ongoing star formation activity in a given star-forming region. In this section, we identify and classify the YSO populations using their infrared excess for a wider field of view around IRAS 17599–2148. Previously, Dewangan et al. (2012) also presented the photometric analysis of point-like sources in the IRAS 17599–2148 region, which was restricted only near the BN. In the following, we give a brief description of YSO identification and classification schemes adopted in this work.

1. In this scheme, the GLIMPSE-MIPSGAL color–magnitude diagram ([3.6]–[24]/[3.6]) is used to identify the different stages of YSOs (Guieu et al. 2010; Rebull et al. 2011; Dewangan et al. 2015a), where the sources have detections in the MIPSGAL 24 μm and GLIMPSE 3.6 μm bands. The 24 μm image is saturated near the *IRAS* position; therefore, this scheme is not used to trace YSOs near the *IRAS* position (see Figure 1(a)). Following the conditions given in Guieu et al. (2010), the boundary of different stages of YSOs is also highlighted in Figure 9(a). In our selected region, we find 170 sources that have detections in both the 3.6 and 24 μm bands. We identify 39 YSOs (4 Class I; 7 Flat-spectrum; 28 Class II) and 131 Class III sources. Furthermore, Figure 9(a) exhibits the boundary of possible contaminants (i.e., galaxies and diskless stars; also see Figure 10 in Rebull et al. 2011). We also find that our identified YSO populations are free from the contaminants. We also identify an embedded source in the IRDC, which is detected at wavelengths longer than 3.6 μm and is designated as MG008.2845+00.1664 in the MIPSGAL photometry catalog (Gutermuth & Heyer 2015). The source has 4.5–24 μm band photometry and is a YSO candidate with a color ($m_{8.0}$–m_{24}) of 3.54 mag.

2. In this scheme, the GLIMPSE color–color diagram ([3.6]–[4.5] vs. [5.8]–[8.0]) of sources is employed that has detections in all four GLIMPSE bands. Following the Gutermuth et al. (2009) schemes, YSOs and various possible contaminants (e.g., broad-line active galactic nuclei, PAH-emitting galaxies, shocked emission blobs/knots, and PAH-emission-contaminated apertures) are identified in our selected region. The possible contaminants are also removed from the selected YSOs. Furthermore, these YSOs are classified into different evolutionary stages based on their slopes of the *Spitzer*-GLIMPSE SED ($\alpha_{3.6-8.0}$) computed from 3.6 to 8.0 μm (i.e., Class I [$\alpha_{3.6-8.0} > -0.3$], Class II [$-0.3 > \alpha_{3.6-8.0} > -1.6$], and Class III [$-1.6 > \alpha_{3.6-8.0} > -2.56$]; e.g., Lada et al. 2006). The GLIMPSE color–color diagram ([3.6]–[4.5] vs. [5.8]–[8.0]) is shown in Figure 9(b). More details on the YSO classifications can be found in the work of Dewangan & Anandarao (2011, and references therein). This scheme leads to 15 YSOs (5 Class I; 10 Class II), 2282 photospheres, and 288 contaminants.

3. In this scheme, the color–color space ([4.5]–[5.8] vs. [3.6]–[4.5]) of sources is used that has detections in the first three GLIMPSE bands (except the 8.0 μm band). The color conditions, $[4.5]-[5.8] \geqslant 0.7$ and $[3.6]-[4.5] \geqslant 0.7$, are adopted to select protostars, as given in Hartmann et al. (2005) and Getman et al. (2007). A total of 11 protostars are found in our selected region (see Figure 9(c)).

4. In this scheme, the color–magnitude space ($H-K/K$) is adopted for selecting additional YSOs. To find a color condition, we explored the color–magnitude space of the nearby control field (size $\sim 5' \times 5'$; central coordinates: $\alpha_{J2000} = 18^{h}02^{m}20\overset{s}{.}7$, $\delta_{J2000} = -21°50'31\overset{''}{.}1$) and selected a color $H-K$ value (i.e., $\sim$2.2) that separates large $H-K$ excess sources from the rest of the population. Considering this color $H-K$ cutoff criterion, 409 embedded YSOs are identified in our selected region (see Figure 9(d)).

Finally, all these schemes give us a total of 474 YSOs in our selected region (as shown in Figure 1). The positions of all these YSOs are shown in Figure 10(a). Several embedded sources are detected toward the EFS.

3.5.2. Study of Distribution of YSOs

The spatial distribution of young stellar populations is often examined using their surface density analysis (e.g., Gutermuth et al. 2009; Bressert et al. 2010), which allows us to infer the young stellar clusters. Previously, using the nearest-neighbor (NN) technique, Dewangan et al. (2012) also obtained the surface density map of YSOs in the IRAS 17599–2148 region, which was studied only near the BN. The surface density map can be generated by dividing the selected field using a regular grid and computing the surface density of YSOs at each grid point. The surface number density at the jth grid point is defined by $\rho_j = (n-1)/A_j$ (e.g., Casertano & Hut 1985), where A_j represents the surface area defined by the radial distance to the $n = 6$ NN. Following this procedure, we generated the surface density map of all 474 selected YSOs, using a 5″ grid and six NNs at a distance of 4.2 kpc. In Figure 10(b), the resultant surface density contours of YSOs are presented. The contour levels are drawn at 4, 6, 9, 15, and 25 YSOs pc^{-2}, increasing from the outer to the inner regions. The YSO clusters are mainly seen toward the IRDC and the BN (see Figure 10(b)). The star formation activity is found toward all the condensations as traced in the *Herschel* column density map.

We also obtained the clustered populations from distributed sources using a statistical analysis of YSOs. We estimated an empirical cumulative distribution (ECD) of YSOs as a function of NN distance (see Chavarría et al. 2008; Gutermuth et al. 2009; Dewangan & Anandarao 2011, for more details). In the ECD analysis, a cutoff length (also referred to as the distance of inflection d_c) is selected for delineating the low-density/distributed populations. For the present case, we selected a cutoff distance of $d_c \sim 44''$ (0.9 pc at a distance of 4.2 kpc). The ECD analysis provided a clustered fraction of about 72% YSOs (i.e., 344 from a total of 474 YSOs).

4. DISCUSSION

On a wider field of view around IRAS 17599–2148, an EFS (extension $\sim$21 pc) has been traced in the *Herschel* continuum images. In Section 3.1.1, we mentioned the presence of a continuous velocity structure in the direction of IRAS 17599–2148 and presented evidence of the existence of the EFS. Considering the molecular and ionized gas velocities, the EFS harbors the IRDC and a BN associated with the H II region

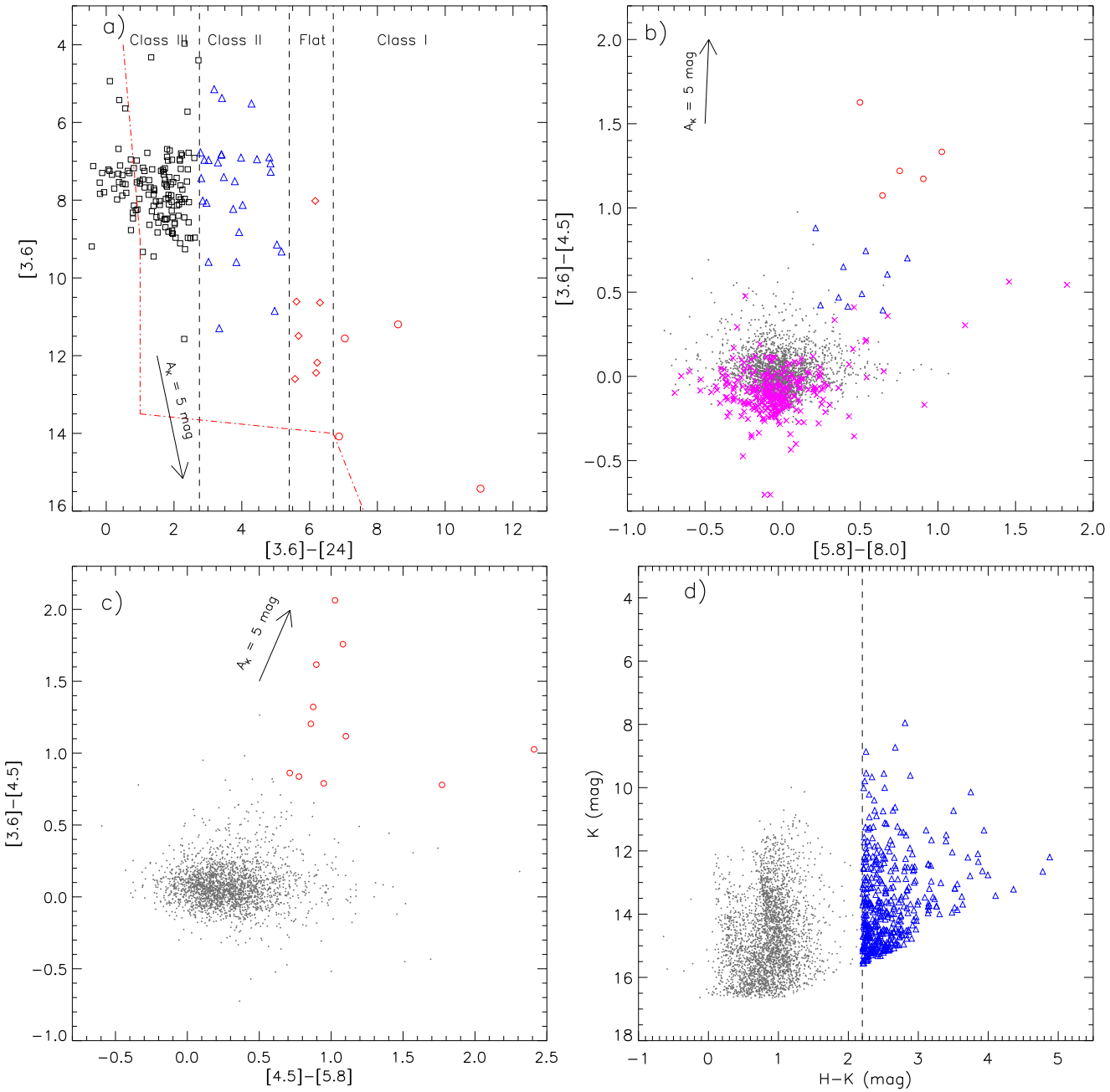

Figure 9. Selection of embedded young stellar population within the region probed in this paper (see Figure 2). (a) Color–magnitude diagram ([3.6]–[24] vs. [3.6]) showing the YSOs belonging to different evolutionary stages (see dashed lines). These sources are detected in the GLIMPSE 3.6 μm and the MIPSGAL 24 μm bands (see the text for more details). The YSOs and contaminated candidates (galaxies and diskless stars) are separated by a dot-dashed curve (see Rebull et al. 2011 for more details). The flat-spectrum and Class III sources are designated by diamonds and squares, respectively. (b) Color–color diagram ([3.6]–[4.5] vs. [5.8]–[8.0]) of sources detected in the four GLIMPSE bands. The cross shows the PAH-emission-contaminated apertures (see the text). (c) Color–color diagram ([3.6]–[4.5] vs. [4.5]–[5.8]) using the first three GLIMPSE band detections (except the 8.0 μm image). (d) Color–magnitude diagram (H–K/K) of the sources observed in the NIR bands. In all the panels, Class I and Class II YSOs are marked by red circles and open blue triangles, respectively. In the last three panels, the gray dots refer to the stars with only photospheric emissions. In the NIR H–K/K space, we have shown only 3001 out of 33,984 stars with photospheric emissions. In the first three panels, the extinction vectors are drawn using the average extinction laws from Flaherty et al. (2007). The positions of all the identified YSOs are shown in Figure 10(a).

IRAS 17599–2148/G8.14+0.23. The ATLASGAL sources at 870 μm (i.e., a chain of dense clumps/cores) are exclusively found toward the IRDC and the BN, tracing dense regions qualitatively. In Section 3.2, using *Herschel* data analysis, the physical conditions (column density and temperature) have been inferred in the region around IRAS 17599–2148. In the *Herschel* temperature map, the IRDC is traced with cold gas (without any radio detection), while the BN is seen with warmer gas, indicating a temperature gradient. We found higher temperatures toward the waist of the BN, which is part of the H II region. This implies that the waist of the BN is heated directly by massive stars that are embedded in dense gas as traced by NH_3 emission. Based on the temperature distribution in the *Herschel* temperature map, the BN is clearly distinguished from the IRDC. This immediately suggests the presence of two distinct environments within the EFS. In our selected region, the *Herschel* column density map reveals 12 clumps. We find at least six massive clumps (IDs: 1–5 and 10;

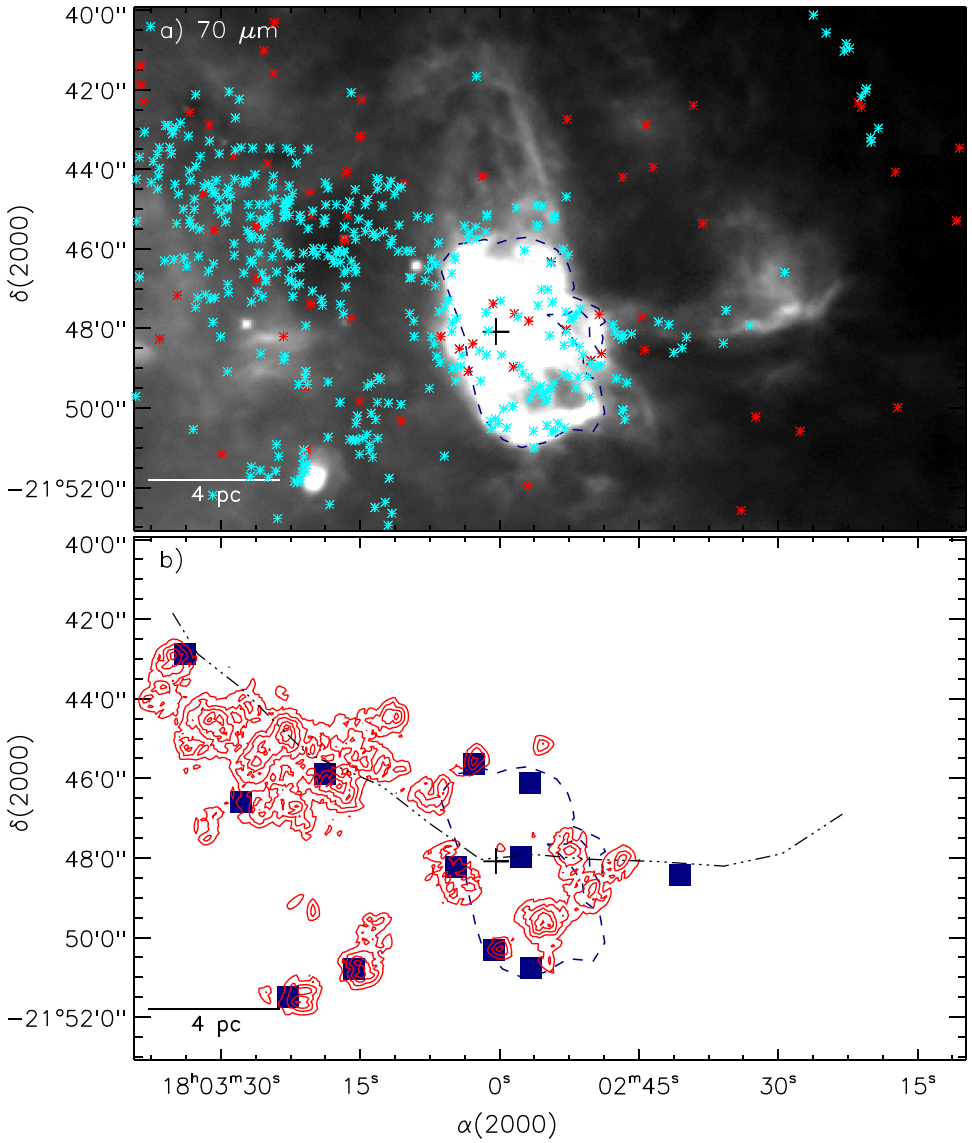

Figure 10. Spatial distribution of YSOs identified within the region probed in this paper using the NIR and MIR data. (a) The asterisks represent the identified YSOs, which are overlaid on the 70 μm image. The YSOs selected using the GLIMPSE and MIPSGAL bands (see the first three panels in Figure 9) are shown by red color, whereas the cyan asterisks represent the YSOs identified using the NIR bands (see Figure 9(d)). (b) Surface density contours (in red) of all the identified YSOs. The contours are shown at 4, 6, 9, 15, and 25 YSOs pc^{-2}, from the outer to the inner side. The filled squares represent the positions of the identified *Herschel* clumps (see Table 1). A tight spatial association between YSO clusters and clumps is evident. A BN is also highlighted in both panels similar to the one shown in Figure 4. An EFS is highlighted by a dot-dashed curve. The position of IRAS 17599–2148 (plus sign) is shown in both panels. In both panels, the scale bar at the bottom left corner corresponds to 4 pc (at a distance of 4.2 kpc). Star formation activities are revealed toward the IRDC and BN (see text for details).

$M_{\rm clump} \sim 777$–$7024\,M_{\odot}$) associated with the filamentary structure, and two of them (IDs: 1–2) are located at the waist of the BN. Four additional clumps (IDs: 6–8 and 12) are also identified at the edges of the BN. All 12 clumps have higher self-gravitating pressure values (i.e., (2.1–29.2) $\times 10^{-10}$ dynes cm^{-2}) and smaller $t_{\rm ff,sph}$ values (i.e., 0.4–0.77 Myr), indicating the signature of the early phase of star formation within the clumps. Based on availability of the line parameters toward four clumps (IDs: 1–4), the virial parameters ($M_{\rm vir}$/$M_{\rm clump}$) for these clumps are less than 1, suggesting that these clumps are prone to collapse. Based on availability of $T_{\rm kin}$, two (IDs: 1–2) out of these four clumps have higher Mach numbers ($\sigma_{\rm NT}/a_s$) (i.e., 5 and 5.8), indicating that the clumps are dominated by nonthermal motions (such as outflows from YSOs). These clumps appear supersonic. All these results favor that the fragmentation occurred within the filaments, which leads to several clumps with higher column densities. Indirectly, these clumps show the signatures of ongoing star formation activities.

In the era of ATLASGAL and *Herschel* surveys, the identification of elongated filaments and the formation of clumps in these filaments have received much attention (e.g., Schneider et al. 2012; Ragan et al. 2014; Contreras et al. 2016; Li et al. 2016, and references therein). The large-scale filaments are likely to be unstable to radial collapse and fragmentation. The spacing of the clumps in the filamentary cloud is often explained by the "sausage" instability produced during the gravitational collapse of a cylinder (Chandrasekhar & Fermi 1953; Nagasawa 1987). More recently, Contreras et al. (2016) studied fragmentation in five filamentary molecular clouds using data from the ATLASGAL 870 μm, *Spitzer*, and Millimetre Astronomy Legacy Team 90 GHz (MALT90)

surveys and also suggested the observed separation of the clumps via the "sausage" instability theory. In this work, the presence of clumps (or a chain of dense clumps/cores) in the EFS could be explained by this instability theory. However, in order to validate the theoretical predictions, high-resolution molecular line data toward the elongated structure are required.

The distribution of YSO clusters traces the star formation activities. In Section 3.5.2, the YSO clusters are found toward the clumps in the EFS. The association of clumps and YSO clusters is evident, illustrating further confirmation of star formation within the clumps. Additionally, the spatial distribution of YSO clusters is also seen at the edges of the BN. Considering the spatial locations of the clusters, star formation appears more intense toward the IRDC. Note that the IRDC contains many deeply embedded YSOs without any ionized emission. The ionized emission is exclusively associated with the most massive clump, which is located at the waist of the BN. A bipolar appearance of IRAS 17599–2148 could be explained due to the ionizing feedback from the O6.5–O6 type star. The position–velocity analysis of the gas kinematics of CO(3–2) suggests the signature of an expanding H II region with an expansion velocity of the gas of $\sim$4.5 km s^{-1}. Dewangan et al. (2012) estimated the dynamical or expansion age of the H II region to be $\sim$1.6 Myr. The average ages of Class I and Class II YSOs are estimated to be $\sim$0.44 Myr and $\sim$1–3 Myr (Evans et al. 2009), respectively. Hence, star formation in the clumps associated with the edges of the BN could be influenced by the H II region. The H II region is spatially situated far away from the IRDC; therefore, the star formation toward the IRDC is unlikely influenced by the H II region. This argument is also supported by the lower value of pressure of the H II region (i.e., $P_{\rm H\,II} = \mu m_H c_s^2 (\sqrt{3N_{uv}/4\pi\ \alpha_B\ D_s^3}) \approx (8\text{–}5) \times 10^{-11}$ dynes cm^{-2}, where $\mu = 2.37$, c_s is the sound speed of the photoionized gas [=10 km s^{-1}], and α_B is the radiative recombination coefficient [=2.6 $\times$ 10^{-13} cm^3 s^{-1}]) driven by an O6.5–O6 type star at projected distances (D_s) of 8–11 pc, which is very close to $P_{\rm MC}$. The onset stellar cluster formation associated with the IRDC appears to be spontaneous. Combining these results, we notice that different star formation processes have taken place in the BN and the IRDC. The star formation associated with the H II region is likely more evolved compared to the IRDC.

5. SUMMARY AND CONCLUSIONS

The present work deals with a multiscale and multi-wavelength analysis around IRAS 17599–2148, using new observations along with publicly available archival data sets. The goal of this paper is to understand the physical environment and star formation processes around IRAS 17599–2148 on the smaller and larger scales. In the following, the important results of this work are provided.

1. On a larger scale, an EFS is evident in the *Herschel* images, which hosts the IRDC and the H II region IRAS 17599–2148/G8.14+0.23. IRAS 17599–2148 has a bipolar appearance at wavelengths longer than 2 μm. Radio emission is not detected toward the IRDC.
2. High-resolution GMRT radio continuum emissions at 0.61 GHz (beam size $\sim$5.″6 $\times$ 5.″2) and 1.28 GHz (beam size $\sim$2.″8 $\times$ 2.″4) show an extended radio emission, which is located toward the waist of the BN and can be excited by a single star of radio spectral type O6.5–O6.
3. The 1.28 GHz map reveals two radio continuum peaks (cp1 and cp2) toward the single peak seen in the 0.61 GHz map. The radio peaks cp1 and cp2 correspond to a single ionizing star of radio spectral type O8V–O8.5V and O9V–O9.5V, respectively.
4. Within 18″ of the IRAS 17599–2148 position, two radio O spectral type sources and a 6.7 GHz MME (without any radio peak) are traced, indicating the presence of different early evolutionary stages of massive star formation.
5. IRS 1 has been identified as an IRc of the 6.7 GHz MME and is a massive protostar candidate. The GMRT radio continuum map at 1.28 GHz ($1\sigma \sim 0.38$ mJy beam^{-1}) does not trace any radio peak toward IRS 1.
6. The inner circumstellar environment of IRS 1 is mapped using the VLT/NACO adaptive optics K_s and L' observations at resolutions of $\sim$0.″2 and $\sim$0.″1, respectively. Within a scale of 4200 au, IRS 1 has been resolved into at least three point-like sources, and one of them is associated with diffuse emission, which could be a collimated infrared jet.
7. Multiscale and multiwavelength data suggest that IRS 1 could be a genuine massive protostar candidate in a very early evolutionary stage, prior to a UCH II phase. Further detailed studies of IRS 1 are encouraged using high-resolution interferometric observations at longer wavelength.
8. The *Herschel* column density map traces 12 clumps, and their masses vary between 410 and 7024 $M_\odot$. In the selected region around IRAS 17599–2148, these clumps are identified with a range of temperature and column density of about 16–39 K and (0.6–11) $\times$ 10^{22} cm^{-2} ($A_V \sim$ 7–117 mag), respectively.
9. The EFS is associated with at least six massive condensations, indicating the fragmentation of the cloud. This argument is also supported by virial analysis of clumps and their higher values of self-gravitating pressure. The most massive condensation (mass $\sim$7024 $M_\odot$) hosts two radio continuum peaks and the 6.7 GHz MME, which is located at the waist of the BN. At least four condensations are also found at the edges of the BN.
10. In the *Herschel* temperature map, the IRDC is found with cold gas (and the absence of any radio continuum emission), while the BN is associated with warmer gas and is part of the H II region. Based on the temperature distribution and ionized emission, the BN is clearly distinguished from the IRDC. This implies two distinct environments within the EFS.
11. The position–velocity analysis of the gas kinematics of CO(3–2) suggests the signature of an expanding H II region with an expansion velocity of the gas of $\sim$4.5 km s^{-1};
12. In the position–velocity plot of CO(3–2), a noticeable velocity gradient has also been found toward the IRAS 17599–2148 position, indicating the presence of a molecular outflow. The exciting source of the outflow could be the driving source of the H II region and/or the IRc of the 6.7 GHz MME; however, due to the coarse

beam of CO data, we cannot conclusively indicate the powering source of the molecular outflow in this work.

13. The analysis of the MIPSGAL, GLIMPSE, and UKIDSS GPS photometry reveals a total of 474 YSOs. The YSO clusters are spatially seen toward the condensations in the filamentary structure, revealing ongoing star formation. YSOs are also identified at the edges of the BN.
14. A point-like source is seen toward each compact radio continuum peak in the VLT/NACO images. There are no nebular features seen toward these sources in the NACO images. A high-resolution spectroscopic study will be very helpful to confirm the ionizing sources of the radio peaks.

Based on our observed results, we conclude that the fragmentation has occurred within the EFS, which produced several clumps (or a chain of dense clumps/cores) along the structure. Star formation activities are going on within these clumps. These YSOs might have spontaneously formed due to processes not related to the expanding H II region. Massive stars were formed in one of the highest column density and massive clumps, and subsequently, an H II region was originated. This H II region has also been expanded in the surroundings, and its ionizing feedback formed a BN. At the edges of the BN, four additional clumps are also associated with the YSO clusters. The expanding H II region may also have triggered the star formation in the periphery of the nebula.

We thank the anonymous referee for providing constructive comments. The research work at Physical Research Laboratory is funded by the Department of Space, Government of India. This work is based on data obtained as part of the UKIRT Infrared Deep Sky Survey. This publication made use of data products from the Two Micron All Sky Survey (a joint project of the University of Massachusetts and the Infrared Processing and Analysis Center/California Institute of Technology, funded by NASA and NSF) and archival data obtained with the *Spitzer Space Telescope* (operated by the Jet Propulsion Laboratory, California Institute of Technology, under a contract with NASA). We thank the staff of the GMRT, who made the radio observations possible. The GMRT is run by the National Centre for Radio Astrophysics of the Tata Institute of Fundamental Research. I.Z. is supported by the Russian Foundation for Basic Research (RFBR). A.L. acknowledges the CONACYT (México) grant CB-2012-01-1828-41.

REFERENCES

Arce, H. G., Borkin, M. A., Goodman, A. A., Pineda, J. E., & Beaumont, C. N. 2011, ApJ, 742, 105
Baug, T., Ojha, D. K., Dewangan, L. K., et al. 2015, MNRAS, 454, 4335
Becker, R. H., White, R. L., Helfand, D. J., & Zoonematkermani, S. 1994, ApJS, 91, 347
Benjamin, R. A., Churchwell, E., Babler, B. L., et al. 2003, PASP, 115, 953
Beuther, H., Ragan, S. E., Johnston, K., et al. 2015, A&A, 584, 67
Bohlin, R. C., Savage, B. D., & Drake, J. F. 1978, ApJ, 224, 132
Bressert, E., Bastian, N., Gutermuth, R., et al. 2010, MNRAS, 409, 54
Carey, S. J., Noriega-Crespo, A., Price, S. D., et al. 2005, BAAS, 37, 1252
Casali, M., Adamson, A., Alves de Oliveira, C., et al. 2007, A&A, 467, 777
Casertano, S., & Hut, P. 1985, ApJ, 298, 80
Chandrasekhar, S., & Fermi, E. 1953, ApJ, 118, 116
Chavarría, L. A., Allen, L. E., Hora, J. L., Brunt, C. M., & Fazio, G. G. 2008, ApJ, 682, 445
Churchwell, E., Watson, D. F., Povich, M. S., et al. 2007, ApJ, 670, 428
Contreras, Y., Garay, G., Rathborne, J. M., & Sanhueza, P. 2016, MNRAS, 456, 2041
Contreras, Y., Schuller, F., Urquhart, J. S., et al. 2013, A&A, 549, 45
de Villiers, H. M., Chrysostomou, A., Thompson, M. A., et al. 2015, MNRAS, 449, 119
Deharveng, L., Schuller, F., Anderson, L. D., et al. 2010, A&A, 523, 6
Dewangan, L. K., & Anandarao, B. G. 2011, MNRAS, 414, 1526
Dewangan, L. K., Luna, A., Ojha, D. K., et al. 2015a, ApJ, 811, 79
Dewangan, L. K., Ojha, D. K., Anandarao, B. G., Ghosh, S. K., & Chakraborti, S. 2012, ApJ, 756, 151
Dewangan, L. K., Ojha, D. K., Grave, J. M. C., & Mallick, K. K. 2015b, MNRAS, 446, 2640
Dewangan, L. K., Ojha, D. K., Luna, A., et al. 2016, ApJ, 819, 66
Duchêne, G., & Kraus, A. 2013, ARA&A, 51, 269
Dunham, M. K., Rosolowsky, E., Evans, N. J., II, Cyganowski, C., & Urquhart, J. S. 2011, ApJ, 741, 110
Dyson, J. E., & Williams, D. A. 1980, Physics of the Interstellar Medium (New York: Halsted Press)
Evans, N. J., II, Dunham, M. M., Jørgensen, J. K., et al. 2009, ApJS, 181, 321
Flaherty, K. M., Pipher, J. L., Megeath, S. T., et al. 2007, ApJ, 663, 1069
Getman, K. V., Feigelson, E. D., Garmire, G., Broos, P., & Wang, J. 2007, ApJ, 654, 316
Goto, M., Stecklum, B., Linz, H., et al. 2006, ApJ, 649, 299
Griffin, M. J., Abergel, A., Abreu, A, et al. 2010, A&A, 518, L3
Guieu, S., Rebull, L. M., Stauffer, J. R., et al. 2010, ApJ, 720, 46
Gutermuth, R. A., & Heyer, M. 2015, AJ, 149, 64
Gutermuth, R. A., Megeath, S. T., Myers, P. C., et al. 2009, ApJS, 184, 18
Hartmann, L., Megeath, S. T., Allen, L., et al. 2005, ApJ, 629, 881
Hildebrand, R. H. 1983, QJRAS, 24, 267
Kauffmann, J., Bertoldi, F., Bourke, T. L., Evans, N. J., II, & Lee, C. W. 2008, ApJ, 487, 993
Kim, K. T., & Koo, B. C. 2001, ApJ, 549, 979
Lada, C. J., Muench, A. A., Luhman, K. L., et al. 2006, AJ, 131, 1574
Lawrence, A., Warren, S. J., Almaini, O., et al. 2007, MNRAS, 379, 1599
Lenzen, R., Hartung, M., Brandner, W., et al. 2003, Proc. SPIE, 4841, 944
Li, Guang-Xing, Urquhart, J. S., Leurini, S., et al. 2016, A&A, 591, 5
Lucas, P. W., Hoare, M. G., Longmore, A., et al. 2008, MNRAS, 391, 136
MacLaren, I., Richardson, K. M., & Wolfendale, A. W. 1988, ApJ, 333, 821
Mallick, K. K., Kumar, M. S. N., Ojha, D. K., et al. 2013, ApJ, 779, 113
Mallick, K. K., Ojha, D. K., Samal, M. R., et al. 2012, ApJ, 759, 48
Mallick, K. K., Ojha, D. K., Tamura, M., et al. 2015, MNRAS, 447, 2307
Martins, F., Schaerer, D., & Hillier, D. J. 2005, A&A, 436, 1049
Matsakis, D. N., Evans, N. J., II, Sato, T., & Zuckerman, B. 1976, AJ, 81, 172
Minier, V., Conway, J. E., & Booth, R. S. 2001, A&A, 369, 278
Nagasawa, M. 1987, PThPh, 77, 635
Omar, A., Chengalur, J. N., & Anish Roshi, D. 2002, A&A, 395, 227
Ott, S. 2010, in ASP Conf. Ser. 434, Astronomical Data Analysis Software and Systems XIX, ed. Y. Mizumoto, K.-I. Morita, & M. Ohishi (San Francisco, CA: ASP), 139
Poglitsch, A., Waelkens, C., Geis, N., et al. 2010, A&A, 518, L2
Ragan, S. E., Henning, T., Beuther, H., Linz, H., & Zahorecz, S. 2015, A&A, 573, 119
Ragan, S. E., Henning, Th., Tackenberg, J., et al. 2014, A&A, 568, 73
Rathborne, J. M., Garay, G., Jackson, J. M., et al. 2011, ApJ, 741, 120
Rebull, L. M., Guieu, S., Stauffer, J. R., et al. 2011, ApJS, 193, 25
Rousset, G., Lacombe, F., Puget, P., et al. 2003, Proc. SPIE, 4839, 140
Schneider, N., Csengeri, T., Hennemann, M., et al. 2012, A&A, 540, L11
Schuller, F., Menten, K. M., Contreras, Y., et al. 2009, A&A, 504, 415
Shirley, Y. L., Ellsworth-bowers, T. P., Svoboda, B., et al. 2013, ApJS, 209, 2
Simon, R., Jackson, J. M., Rathborne, J. M., & Chambers, E. T. 2006, ApJ, 639, 227
Skrutskie, M. F., Cutri, R. M., Stiening, R., et al. 2006, AJ, 131, 1163
Szymczak, M., Wolak, P., Bartkiewicz, A., & Borkowski, K. M. 2012, AN, 333, 634
Tackenberg, J., Beuther, H., Henning, T., et al. 2012, A&A, 540, 113
Tafalla, M., & Hacar, A. 2015, A&A, 574, 104
Takeuchi, T., Yamamoto, H., Torii, K., et al. 2010, PASJ, 62, 557
Tan, J. C., Beltrán, M. T., Caselli, P., et al. 2014, in Protostars and Planets VI, ed. H. Beuther et al. (Tucson, AZ: Univ. Arizona Press), 149
Tobin, J. J., Looney, L. W., Li, Z.-Y., et al. 2016, ApJ, 818, 73
Urquhart, J. S., Moore, T. J. T., Schuller, F., et al. 2013, MNRAS, 431, 1752
Walsh, A. J., Burton, M. G., Hyland, A. R., & Robinson, G. 1998, MNRAS, 301, 640
Wienen, M., Wyrowski, F., Schuller, F., et al. 2012, A&A, 544, 146
Williams, J. P., de Geus, E. J., & Blitz, L. 1994, ApJ, 428, 693
Xu, J.-L., Li, D., Zhang, C.-P., et al. 2016, ApJ, 819, 117
Zhang, Y., & Tan, J. C. 2011, ApJ, 733, 55
Zinnecker, H., & Yorke, H. W. 2007, ARA&A, 45, 481